

Sample-efficient model-based reinforcement learning for quantum control

Irtaza Khalid,^{1,*} Carrie A. Weidner^{2,†} Edmond A. Jonckheere^{3,‡} Sophie G. Schirmer^{4,§} and Frank C. Langbein^{1,||}

¹*School of Computer Science and Informatics, Cardiff University, Cardiff CF24 4AG, United Kingdom*

²*Quantum Engineering Technology Laboratories, H. H. Wills Physics Laboratory and Department of Electrical and Electronic Engineering, University of Bristol, Bristol BS8 1FD, United Kingdom*

³*Department of Electrical and Computer Engineering, University of Southern California, Los Angeles, California 90007, USA*

⁴*Department of Physics, Swansea University, Swansea SA2 8PP, United Kingdom*



(Received 27 April 2023; accepted 12 September 2023; published 2 October 2023)

We propose a model-based reinforcement learning (RL) approach for noisy time-dependent gate optimization with reduced sample complexity over model-free RL. Sample complexity is defined as the number of controller interactions with the physical system. Leveraging an inductive bias, inspired by recent advances in neural ordinary differential equations (ODEs), we use an autodifferentiable ODE, parametrized by a learnable Hamiltonian ansatz, to represent the model approximating the environment, whose time-dependent part, including the control, is fully known. Control alongside Hamiltonian learning of continuous time-independent parameters is addressed through interactions with the system. We demonstrate an order of magnitude advantage in sample complexity of our method over standard model-free RL in preparing some standard unitary gates with closed and open system dynamics, in realistic computational experiments incorporating single-shot measurements, arbitrary Hilbert space truncations, and uncertainty in Hamiltonian parameters. Also, the learned Hamiltonian can be leveraged by existing control methods like GRAPE (gradient ascent pulse engineering) for further gradient-based optimization with the controllers found by RL as initializations. Our algorithm, which we apply to nitrogen vacancy (NV) centers and transmons, is well suited for controlling partially characterized one- and two-qubit systems.

DOI: [10.1103/PhysRevResearch.5.043002](https://doi.org/10.1103/PhysRevResearch.5.043002)

I. INTRODUCTION

Control of quantum devices for practical applications requires us to overcome a unique set of challenges [1]. One is to find robust controls for noisy systems, where typical noise sources include control and feedback noise, system parameter mischaracterization, measurement and state preparation errors, decoherence, and cross-talk [2]. To achieve scalable, fault-tolerant quantum devices [3–5], control algorithms must produce controls resilient to such noise. Reinforcement learning (RL) approaches appear more likely to find robust controls for certain applications [6] at the cost of requiring a large number of measurements from the quantum device (samples). We propose a model-based RL approach to address this problem.

Typically, a quantum control problem is formulated as an open-loop optimization problem based on a model [1,7–9], which may be constructed *ab initio* or obtained via a process tomography approach. During optimization there is

no interaction between the physical system to be controlled and the control algorithm. The underlying assumption is that the model represents the system sufficiently accurately. This class of control algorithms has low sample complexity (high sample efficiency) represented by the number of optimization function calls until successful termination. The reason for this is generally that an analytical model, in particular gradient information, can be leveraged. This is a strong assumption, at least in the noisy intermediate scale quantum era, where noise impedes perfect characterization of quantum devices. However, the approach has merit, since significant thought goes into modeling and engineering quantum devices [10].

Alternatively, RL seeks an optimal control via interaction with the physical system, building models to various degrees. It successfully addresses challenging, noisy quantum control problems with the promise of inherent robustness [6,11–15]. There are also gradient-free approaches [16] and methods that estimate gradients using variations of automatic differentiation [10,17–20].

RL approaches utilizing only measurements without prior information do not suffer from model bias. Moreover, they usually optimize an average controller performance over the noise in the system, yielding inherently robust controllers [12]. However, this means the number of optimization function calls becomes prohibitively large, and RL's high sample complexity is a core problem limiting its practical applicability [21]. This is not surprising, as without a prior model, little or no information is available to the optimization algorithm, and all information must be obtained via measurements.

*khalidmi@cardiff.ac.uk

†c.weidner@bristol.ac.uk

‡jonckhee@usc.edu

§lw1660@gmail.com

||frank@langbein.org

Despite this inherent restriction, RL has been deployed recently on real quantum devices for parametrized pulse-level gate optimization [22], improving the performance of quantum error-correcting codes [23] and fluxonium gate parameter optimization [24]. In line with forthcoming analysis, the sample complexity of these RL experiments is estimated to be around 10^4 , 10^3 , and 10^4 , respectively, excluding the cost of estimating observables using single-shot measurements. These costs are smaller than direct or *ab initio* applications of RL, which consume around 10^6 samples [21], as the aforementioned works, to differing extents, exploit specific knowledge of the quantum system to frame the problem to be easier to optimize for the RL agent. More specifically, these works use custom RL adaptations for each problem, e.g., fine-tuning solutions already found by other optimization algorithms as the final step during control preparation in Ref. [24], or exploiting some experimental structure that simplifies finding optimal controls in Ref. [22]. In the present paper, we remain generic in our ignorance of the system Hamiltonian during acquisition of optimal controls to demonstrate the general utility of our approach without inducing constraining (and potentially incorrect if not confidently known) biases on the learning problem. We note, however, that there is significant scope for sample-efficiency reductions. For example, the use of our model-based RL algorithm would make RL, in general, extensible to a wider class of quantum control experiments.

In classical RL, high sample complexity is typically addressed using model-based methods, which construct a model from scratch using information obtained from measurements. Such methods result in reduced sample complexity for benchmark problems [25]. They are successful if the model and the measurements (samples) obtained during training possess some generalizability [26,27] that is captured by a function approximator (usually a neural network). However, methods involving universal function approximation of dynamic trajectories are unstable. This is because learning can be hindered by the very large space of trajectories, and interpolating from insufficient sample trajectories can be shallow or incorrect [28]. More importantly, for quantum data it is known that a time-independent Hamiltonian can generate many unitary propagators, so estimating the model may imply learning the entire Hilbert space of propagators for a particular control problem, which is often intractable. This motivates learning the dynamical generator, i.e., the Hamiltonian, instead of the propagators.

In this paper, we propose a model-based RL method for time-dependent, noisy gate preparation where the model is given by an ordinary differential equation (ODE), differentiable with respect to model parameters [29]. ODE trajectories do not intersect [30–32], which constrains the space of potential models for learning and makes learning robust to noise. We parametrize the Hamiltonian by known time-dependent controls and unknown time-independent (system) parameters, which, in addition, makes the model interpretable.

We show that combining the inductive bias from this ODE model with partially correct knowledge (assuming the controls are known but not the time-independent system Hamiltonian) reduces the sample complexity compared to model-free RL by at least an order of magnitude.

It has recently been shown that inductive biases, i.e., encoding the symmetries of the problem into the architecture of the model space, such as the translation equivariance of images in the convolution operation [33], leads to stronger out-of-distribution generalization by the learned model. This is because inductive biases impose strong priors on the space of models such that training involves exploring a smaller subset of the space to find an approximately correct model.

We demonstrate improvement over the sample-efficient soft-actor critic (SAC) model-free RL algorithm [34] for performing noisy gate control in leading quantum computing architectures: nitrogen vacancy (NV) centers (one and two qubits) [35], and transmons (two qubits) [36], subject to dissipation and single-shot measurement noise. We also show that the learned Hamiltonian can be leveraged to optimize the controllers found by our RL method further using gradient ascent pulse engineering (GRAPE) [7,9].

Our approach is similar in spirit to Ref. [37], where a novel Hamiltonian learning protocol via quantum process tomography is proposed for the purpose of model-predictive control. The complete Hamiltonian (including the control and system parts) is identified term by term via a zero-order hold (ZOH) method, where only one term is turned on at a time, e.g., by setting the control parameters to zero, and learned individually using optimization over the Stiefel manifold. As a side remark, a sample complexity advantage to learning the Hamiltonian with quantum control rather than without it has recently been shown [38]. The learned Hamiltonian is then used to obtain a viable control sequence for a variety of state and gate preparation problems for closed (unitary) systems under the influence of initial state preparation errors. While it is possible for our Hamiltonian learning protocol to also learn the full Hamiltonian using the ZOH method, we focus on the problem of improving the sample complexity of RL in this paper through the incorporation of a partially known physics-inspired model. Furthermore, our focus is also directed on the interplay of concurrently learning the model and controlling the system in noisy closed and open system settings.

This paper is organized as follows: In Sec. II we define the open and closed system control problems including our setup to simulate single-shot measurements and the RL control framework, Sec. III describes the model-based version of the RL control framework, and Sec. IV presents numerical studies for some realistic example control problems on the system architectures described above in noisy and ideal settings and how to leverage the learned system Hamiltonian using GRAPE. In the Appendixes, we present additional details and proofs for the results in the main text.

II. THE QUANTUM CONTROL PROBLEM

We briefly introduce the quantum control problem for open and closed quantum systems, and we describe how we estimate the propagators from measurements needed for our RL approach.

A. Closed system dynamics

Consider a quantum system that is represented by an effective Hamiltonian $H(t)$ in the space of complex Hermitian

$n \times n$ matrices,

$$H(\mathbf{u}(t), t) = H_0 + H_c(\mathbf{u}(t), t), \quad (1)$$

where H_0 is the time-independent system Hamiltonian and H_c is the control Hamiltonian parametrized by time-dependent controls $\mathbf{u}(t)$. Its closed-system dynamics are governed by the Schrödinger equation,

$$\frac{dU(\mathbf{u}(t), t)}{dt} = -\frac{i}{\hbar}H(\mathbf{u}(t), t)U(\mathbf{u}(t), t), \quad U(t=0) = \mathbb{1}, \quad (2)$$

where $U(\mathbf{u}(t), t)$ is the unitary propagator representing the state evolution. Its fidelity to realize a target gate U_{target} is

$$F(U_{\text{target}}, U(\mathbf{u}(t), t)) = \frac{1}{n^2} |\text{Tr}[U_{\text{target}}^\dagger U(\mathbf{u}(t), t)]|^2. \quad (3)$$

The control problem to implement U_{target} is

$$\mathbf{u}^*(t^*) = \arg \max_{\mathbf{u}(\bar{t}), t \leq T} F(U_{\text{target}}, U(\mathbf{u}(t), t)), \quad (4)$$

where $\mathbf{u}^*(t^*)$ are the optimized control parameters for an optimized final time $t^* \leq T$.

B. Open system dynamics

For open system dynamics, consider an arbitrary state with density matrix ρ for $\log_d n$ qudits evolving according to the master equation [39,40]

$$\frac{d\rho(t)}{dt} = -\frac{i}{\hbar}[H(\mathbf{u}(t), t), \rho] + \mathcal{L}(\rho(t)), \quad (5)$$

where $\mathcal{L}(t)$ describes the Markovian decoherence and dephasing dynamics (i.e., the environment),

$$\mathcal{L}(\rho(t)) = \sum_d \gamma_d \left(l_d \rho l_d^\dagger - \frac{1}{2} \{l_d^\dagger l_d, \rho\} \right), \quad (6)$$

and l_d is a decoherence operator that can be nonunitary.

To characterize the gate implemented by $\mathbf{u}(t)$, we need to consider the evolution of a complete orthonormal basis of states, $\{\rho_k\}_{k=1}^{n^2}$. For this we introduce the Liouville superoperator matrix \mathbf{X} that acts on an arbitrary vectorized state ρ (e.g., obtained by stacking the matrix columns) to produce the evolution

$$\rho(t) = \mathbf{X}(t)\rho(t=0). \quad (7)$$

This is equivalent to the tensor-matrix evolution [41]

$$\rho(t)_{mn} = \sum_{\mu, \nu} X_{nm, \nu\mu}(t) \rho_{\mu\nu}(t=0). \quad (8)$$

$X_{nm, \nu\mu}(t)$ is a fourth order tensor (used to refer to multidimensional arrays in this context) form of $\mathbf{X}(t)$ that encodes the evolution of the state element $\rho_{\mu\nu}$.

Thus, similar to Eq. (2), we define a superoperator $X(\mathbf{u}(t), t)$ which encodes the evolution of $\{\rho_k\}_{k=1}^{n^2}$ and follows the linear ODE:

$$\frac{d\mathbf{X}(\mathbf{u}(t), t)}{dt} = -\frac{i}{\hbar}(\mathbf{L}_0 + i\mathbf{L}_1)\mathbf{X}(\mathbf{u}(t), t), \quad \mathbf{X}(t=0) = \mathbb{1} \quad (9)$$

where $\mathbf{L}_0, \mathbf{L}_1$ represent the superoperator version of the commutator map $[H(\mathbf{u}(t), t), \cdot]$, and $\mathcal{L}(\cdot)$ denotes the Markovian decoherence and dephasing dynamics.

We factorize out an imaginary prefactor i to the left in Eq. (9) to unify the ODE for open and closed system dynamics. For $\mathcal{L} \equiv \mathbf{0}$, the above reduces to the closed system dynamics of Eq. (2). For open dynamics, to be faithful to experimental limitations, we implement single-shot noise when estimating the gate, i.e., process tomography. We transform the superoperator $X_{nm, \nu\mu}$ to the Choi matrix $\Phi/\text{Tr}[\Phi]$ that is given by index reshuffling or partial transpose (and more formally a contravariant-covariant change of coordinates) [41,42],

$$\Phi_{nm, \mu\nu} = X_{vm, \mu n}. \quad (10)$$

In Sec. IV, we use this for open and closed dynamics. Estimating Φ is possible using ancilla-assisted quantum process tomography (AAPT) and the Choi-Jamiolkowski isomorphism [43–45] for $2 \log_d n$ -qudit states and $\log_d n$ -qudit gates. Analogously to the above, Φ has a matrix version Φ . In this paper, we decompose Φ over a generalized $\mathfrak{su}(n^2)$'s algebra basis $\{P_k\}_{k=1}^{n^4-1}$, e.g., Gell-Mann matrices [46],

$$\frac{\Phi}{\text{Tr}[\Phi]} = \frac{\mathbb{1}}{n^2} + \sum_{k=2}^{n^4-1} q_k P_k \quad (11)$$

whose coefficients are

$$q_k = \frac{\text{Tr}[P_k \Phi]}{\text{Tr}[\Phi]} \in [-1, 1]. \quad (12)$$

q_k can be modeled as a binomial random variable $\text{Bin}(M, p_k)$ with probability $p_k = \frac{1}{2}(1 + q_k)$, where M is the number of single-shot (Bernoulli) measurements [47]. The Gell-Mann matrices are a generalization of the Pauli matrices, and the corresponding physical measurement operations are akin to measuring qudit energy levels in an informationally complete basis.

We measure the faithfulness of the implemented gate $\Phi(\mathbf{u}(t), t)$ with respect to the target gate (as another Choi state) Φ_{target} using the generalized state-fidelity [48],

$$F(\Phi(\mathbf{u}(t), t), \Phi_{\text{target}}) = \frac{\text{Tr}[\Phi(\mathbf{u}(t), t)\Phi_{\text{target}}]}{\text{Tr}[\Phi(\mathbf{u}(t), t)]\text{Tr}[\Phi_{\text{target}}]} = \frac{1}{n^4} + \sum_{k=2}^{n^4-1} q_k^{\text{target}} q_k. \quad (13)$$

Analogously to the closed case, the open control problem is to find an optimal control $\mathbf{u}^*(t^*)$ for an optimal final time $t^* \leq T$ (with T being the fixed upper bound), such that

$$\mathbf{u}^*(t^*) = \arg \max_{\mathbf{u}(\bar{t}), t \leq T} F(\Phi(\mathbf{u}(t), t), \Phi_{\text{target}}). \quad (14)$$

C. Discretization

The exact solution of the time-dependent general dynamics discussed in Eq. (14) is given by the time-ordered operator

$$\mathbf{E}(t^*, \mathbf{u}^*(t^*)) = \mathcal{T} \exp \left(\int_0^{t^*} dt' -\frac{i}{\hbar} \mathbf{G}(t', \mathbf{u}^*(t')) \right)$$

for a unitary or Lindbladian generator \mathbf{G} . In practice, we solve for a piecewise constant version of the dynamics represented by N fixed steps of $\Delta t = T/N$ of the final time T . Thus,

$\mathbf{E}(\mathbf{u}(t), t)$ is discretized, which amounts to fixing $\mathbf{u}(t) = \mathbf{u}_m$ to be constant for each time step such that $\mathbf{u}_m \in \mathbb{C}^{m \times C}$ is a finite-dimensional array where C is the number of controls per time step in the vector u_l parametrizing $H_c(u_l, t_l)$ and m is the number of total time steps in the pulse, with $m \leq N$ for a maximum number of pulse segments N . The propagator is

$$\mathbf{E}(t, \mathbf{u}(t)) := \mathbf{E}(\mathbf{u}_m) = \prod_{l=1}^m \exp\left(-\frac{i}{\hbar} \Delta t \mathbf{G}(t_l, \mathbf{u}(t_l))\right). \quad (15)$$

The control problems in Eqs. (4) and (14) are equivalent to

$$\mathbf{u}_m^* = \arg \max_{\mathbf{u}_m = [u_1, \dots, u_m] \in \mathbb{X}, m \leq N} \mathcal{F}(\Phi(\mathbf{E}(\mathbf{u}_m)), \Phi(\mathbf{E}_{\text{target}})) \quad (16)$$

for a fidelity \mathcal{F} and the time. \mathbf{u}_m is constrained to some maximum and minimum values given by $\mathbb{X} = \{\mathbf{u}_m : \forall c, l \ u_{\min} \leq u_{cl} \leq u_{\max} \in \mathbb{C}\}$. The constraints are applied separately to the real and imaginary parts of the components of \mathbf{u}_m .

III. MODEL-BASED REINFORCEMENT LEARNING CONTROL

We give a brief overview of RL, followed by explaining our model-based RL approach. An excellent introduction can be found in Ref. [21].

A. Reinforcement learning for quantum control

The RL problem is usually treated as a sequential Markov decision problem (MDP) on the space of states, actions, transition probabilities, and rewards: $(\mathcal{S}, \mathcal{A}, \mathcal{P}, \mathcal{R})$. This describes an environment for consecutive one-step transitions, indexed by $k = 1, 2, \dots$, from current state $\mathbf{s}_k \in \mathcal{S}$ to next state $\mathbf{s}_{k+1} \in \mathcal{S}$ if an RL agent executes action $\mathbf{a}_k \in \mathcal{A}$, yielding immediate scalar reward $r_k \in \mathcal{R}$. The environment is generally probabilistic, so $\mathcal{P}(\mathbf{s}_{k+1} | \mathbf{s}_k, \mathbf{a}_k)$ is the probability that the agent is in state \mathbf{s}_{k+1} after executing \mathbf{a}_k in state \mathbf{s}_k . An RL agent follows a policy function that is represented by a conditional probability distribution $\pi(\mathbf{a}_k | \mathbf{s}_k)$: the probability of taking action \mathbf{a}_k after observing the state \mathbf{s}_k .

The quantum control problem can be represented as an RL problem by sequentially constructing the control amplitudes as actions, using the unitary propagator that the control implements as the state with the reward as the fidelity:

$$\mathbf{a}_k = u_k, \quad (17a)$$

$$\mathbf{s}_k = \prod_{l=1}^k \exp\left(-\frac{i}{\hbar} \Delta t \mathbf{G}(t_l, u_l)\right), \quad (17b)$$

$$r_k = \mathcal{F}(\Phi(\mathbf{E}(\mathbf{u}_k)), \Phi(\mathbf{E}_{\text{target}})). \quad (17c)$$

As this is deterministic, the probabilities \mathcal{P} are trivial, and we have a simple environment function $\mathcal{E} : \mathcal{S} \times \mathcal{A} \rightarrow \mathcal{S} \times \mathcal{R}$, mapping the current state and action (s, a) to the next state and reward (s', r) . In model-free RL (see Algorithm 1), a discounted sum of expected rewards, called the returns,

$$\eta(\pi) := \mathbb{E}_{\mathbf{a}_k \sim \pi} \left[\sum_{k=0}^{\infty} \gamma^k r_k \right], \quad (18)$$

is maximized, where $\mathbb{E}_{x \sim P}[\cdot] = \int_{\mathcal{X}} dx P(x)[\cdot]$ is the expectation operator and $0 \leq \gamma \leq 1$ is a discount factor.

Algorithm 1. Reinforcement learning loop.

```

1 Initialize empty data set  $\mathcal{D}$ , parametrized random policy
 $\pi_\theta, k \leftarrow 0$ 
2 Observe initial state  $s_0$ 
3 While  $k < T/\Delta t$  do
4   Execute  $\mathbf{a}_k \leftarrow \pi_\theta(\cdot | \mathbf{s}_k)$ 
5   Observe  $\mathbf{s}_{k+1}, r_k \leftarrow \mathcal{E}(\mathbf{s}_k, \mathbf{a}_k)$ 
6   Store  $\mathcal{D} \leftarrow \mathcal{D} \cup \{(\mathbf{s}_k, \mathbf{s}_{k+1}, \mathbf{a}_k, r_k)\}$ 
7    $k \leftarrow k + 1$ 
   // if require update: perform model-free update of
   // parameters (e.g., policy  $\pi_\theta$ )

```

However, Refs. [34,49] observe that adding an entropy maximizing term for the policy $\pi(\mathbf{a}_k | \mathbf{s}_k)$ to the optimization objective encourages exploration of the state space \mathcal{S} , improves the learning rate of the agent, and reduces the relative number of samples needed, compared to other standard RL algorithms. The maximum entropy objective or the entropy-regularized cumulative reward function J for N steps is

$$J(\pi) = \sum_{k=0}^N \gamma^k \mathbb{E}_{(\mathbf{s}_k, r_k) \sim \mathcal{E}_\pi} [r_k + \alpha J_1(\mathbf{s}_k)], \quad (19)$$

where \mathcal{E}_π represents the environment's state-action probability distribution induced by the policy π , α is an optimizable temperature parameter (signifying the importance of exploration in the objective), and $J_1(\mathbf{s}_k)$ is the entropy of the policy function $\pi(\cdot | \mathbf{s}_k)$ conditional on the k th state \mathbf{s}_k ,

$$J_1(\mathbf{s}_k) = -\mathbb{E}_{x \sim \pi(\cdot | \mathbf{s}_k)} [\log(\pi(x | \mathbf{s}_k))]. \quad (20)$$

Thus, the RL control problem becomes a problem of finding the optimal control policy π^* given by

$$\pi^* = \arg \max_{\pi} J(\pi). \quad (21)$$

This is exactly solvable for tabular MDPs using dynamic programming and heuristically with neural network function approximation for continuous MDPs.

B. Model-based reinforcement learning

In this paper, we use the soft actor-critic (SAC) algorithm [34] as our base (model-free) RL algorithm. For brevity, we only highlight parts of SAC relevant to us. A detailed description can be found in the original paper [34]. We use a neural network policy function $\pi_\theta(\mathbf{a}_k | \mathbf{s}_k)$, with the optimizable parameters θ , as the actor and the state-action value function $Q_\phi(\mathbf{s}_k, \mathbf{a}_k) = \mathbb{E}_{(\mathbf{s}_k, \mathbf{a}_k) \sim \mathcal{E}_\pi} [\sum_{k=0}^{\infty} \gamma^k [r(\mathbf{s}_k, \mathbf{a}_k) + \alpha J_1(\mathbf{s}_k)]]$ as the neural network critic with parameters ϕ . Both π and Q are simple multilayer perceptrons. In essence, the critic is used to reduce the high variance in the reward function due to the nonstationary nature of the MDP. It is trained by having its predictions match the estimated \hat{Q} values obtained for some data $\{\mathbf{s}_k, \mathbf{s}_{k+1}, \mathbf{a}_k, r_k\}_{k=1}^b$ obtained from a b -length rollout (number of interactions) with \mathcal{E} . The actor is trained by minimizing the loss function

$$J'(\pi_\theta) = \mathbb{E}_{(\mathbf{s}_k, \mathbf{a}_k) \sim \mathcal{E}_{\pi_\theta}} [\alpha \log \pi_\theta(\mathbf{a}_k | \mathbf{s}_k) - Q_\phi(\mathbf{s}_k, \mathbf{a}_k)], \quad (22)$$

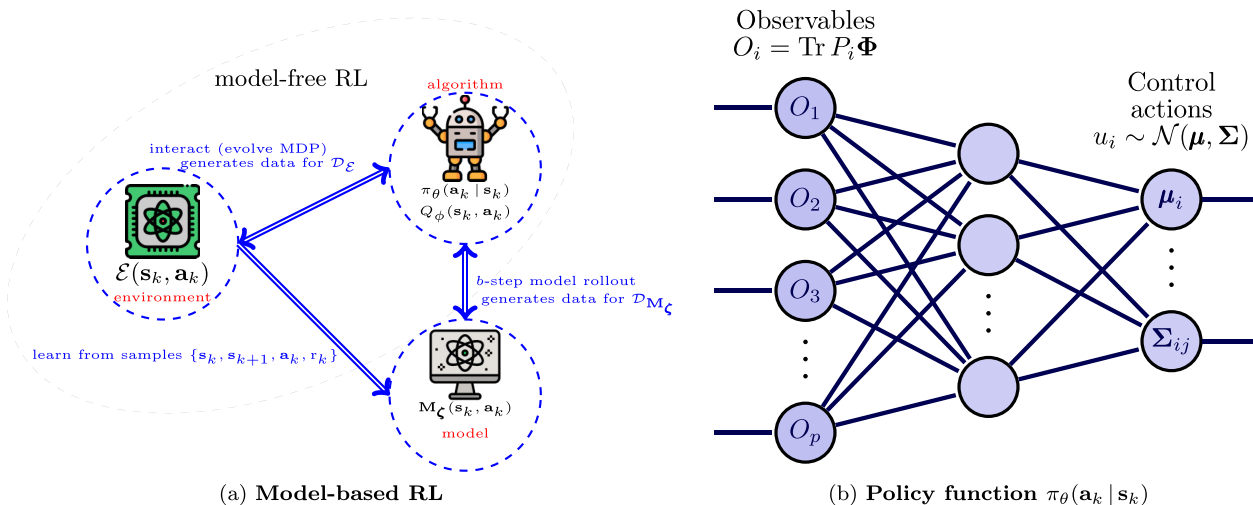


FIG. 1. A schematic of model-based RL is given in (a). The arrowhead implies the direction of affect of the edge between a source and a sink node. The agent or policy function π_θ interacts with the RL environment modeled as MDP to collect data $\{s_k, s_{k+1}, \mathbf{a}_k, r_k\}$. This encompasses model-free RL. The data are then used to train the model $M_\zeta(s_k, \mathbf{a}_k)$. The model is trained until some quality measure such as the validation prediction error on some untrained-upon data from the environment plateaus, indicating that the training is complete. Then, it is used to generate synthetic data through a b -step rollout in which the policy interacts with the model b times. The policy parameters θ (and the state-action value function parameters ϕ) are optimized using the real and model generated data. In (b), we visualize the policy inputs as the gate-characterizing observables (unitary or Lindblad) about the Choi matrix Φ given by Eq. (12), and the tunable outputs are the parameters of a multivariate Gaussian distribution, i.e., the mean μ and covariance Σ . The controls u_i are drawn from $\mathcal{N}(\mu, \Sigma)$.

which is equivalent to maximizing J in Eq. (19). For SAC, this policy optimization is carried out heuristically using neural networks to approximate the policy function π_θ . We define the number of agent-environment interactions needed to find an approximately optimal policy π^* as the *sample complexity*. Moreover, the policy outputs parametrize the mean and covariance μ, Σ of a multivariate Gaussian $\mathcal{N}(\mu, \Sigma)$ from which the control vector \mathbf{u} is drawn. For the quantum control problem in Eq. (16), we are usually just concerned with finding an optimal action sequence \mathbf{u}^* producing the maximum intermediate reward r_k rather than the optimal policy function π^* which can be produced by a suboptimal policy, too.

SAC can be augmented to incorporate a model $M_\zeta(s_k, \mathbf{a}_k)$ that approximates the dynamics of $\mathcal{E}(s_k, \mathbf{a}_k)$ using the policy's interaction data \mathcal{D} [27] where ζ are the model's learnable parameters. The model acts as a proxy for the environment and allows the policy to do MDP rollouts (steps) to augment the interaction data. For this to work, the dynamics obtained from interacting with M_ζ must be close enough to the true dynamics of \mathcal{E} to allow the policy to maximize J . By improving the returns $\hat{\eta}(\pi)$ on the model M_ζ by at least a tolerance factor that depends on this dynamical modeling error, the policy's true returns $\eta(\pi)$ on the environment are guaranteed to improve ([27], see Appendix C for a detailed mathematical discussion). See Fig. 1 for an illustration of model-based RL. A good choice of the model function class, therefore, can impose strong and beneficial constraints on the space of possible predicted dynamics and thus lead to a smaller modeling error and returns' tolerance factor or allow the model to reduce the tolerance factor greatly after consuming an appropriate amount of training data.

Our choice of the model's functional form is motivated by the two ideas presented in the Introduction: (a) incorporating correct partial knowledge about the physical system in the

model ansatz parameters; (b) encoding the problem's symmetries and structure into model predictions as function space constraints. For the system in Eq. (1), we assume that the controls are partially characterized to address (a). Specifically, its time-dependent control structure H_c is known. We achieve (b) by parametrizing the system Hamiltonian $H_0^{(L)}(\zeta)$ with learnable parameters ζ , where L is the number of qubits. We make the model M_ζ a differentiable ODE whose generator is interpretable and has the form

$$H_\zeta(\mathbf{u}(t), t) = H_0^{(L)}(\zeta) + H_c(\mathbf{u}(t), t) = \sum_{l=1}^{n^2} \zeta_l P_l + H_c(\mathbf{u}(t), t), \quad (23)$$

where $\zeta_l = \text{Tr}[P_l H_0(t)] \in [-1, 1]$ are real. Generally, like the Choi state, $H_0/\text{Tr}[H_0]$ admits an arbitrary decomposition in terms of a basis $\{P_l\}_{l=1}^{n^2-1}$ of the SUn 's Lie algebra. Analogously, for an open system, we parametrize the time-independent part of any dissipation dynamics in addition to the system Hamiltonian using an $SU(n^2)$ algebra parametrization: $\mathbf{G}_0^{(L)}(\zeta^{\text{diss}}) = \sum_l \zeta_l^{\text{diss}} P_l$ in the full generator \mathbf{G}_ζ .

The model is trained by minimizing the regression loss for single time-step predictions using data uniformly sampled, $D \sim \mathcal{D}$, where \mathcal{D} represents the entire data set,

$$L_{\text{model}}(D) = \sum_D [M_\zeta(s_k, \mathbf{a}_k) - s_{k+1}]^2. \quad (24)$$

To understand why a differentiable ODE ansatz is a good choice for the model, we need to define an ODE path that is given by $\phi_t : \mathbf{E}(0) \xrightarrow{H_\zeta} \mathbf{E}(T)$ generated by H_ζ for some time $t \in [0, T]$ and propagator \mathbf{E} . The ansatz is a good choice because of the following two properties of ODE paths: (a) they do not intersect, and (b) if paths $\phi_0^{(A)}, \phi_0^{(B)}$ start close compared

Algorithm 2. Learnable Hamiltonian model-based soft actor critic (LH-MBSAC).

Input :
 H_c control Hamiltonian [time-dependent part of $H(t)$ in Eq. (1)]
 $T, \Delta t, M$ max time, time-step size, number of single-shot measurements [if open system to estimate Φ using Eq. (12)]
 $\mathbf{E}_{\text{target}}$ target gate
 W, C, b, tol Epochs, time steps, rollout length, validation loss tolerance (which is a problem-specific hyperparameter)

Output:
 \mathbf{u}^* Approximately optimal 2D array of controls that solves Eq. (16)
 θ, ϕ, ζ Optimized parameters of the policy, critic, and learned model

- 1 Initialize empty environment data set $\mathcal{D}_{\mathcal{E}}$, model data set $\mathcal{D}_{\mathbf{M}_{\zeta}}$, random policy π_{θ}
// collect random model training data
- 2 Populate $\mathcal{D}_{\mathcal{E}}$ using uniform random policy π_{θ} with Algorithm 1 ▷ randomly explore the environment \mathcal{E} state space without updates
- 3 **for** W epochs **do**
// Train model
- 4 Sample a batch of training and validation data $D_{\text{train}}, D_{\text{val}} \sim \mathcal{D}_{\mathcal{E}}$ and minimize $L_{\text{model}}(D_{\text{train}})$ in Eq. (24)
- 5 **for** C time steps **do**
// agent-environment interaction
- 6 Execute $\mathbf{a}_k \leftarrow \pi_{\theta}(\cdot | \mathbf{s}_k)$, observe $\mathbf{s}_{k+1}, \mathbf{r}_k \leftarrow \mathcal{E}(\mathbf{s}_k, \mathbf{a}_k)$, and store data $\mathcal{D}_{\mathcal{E}} \cup \{(\mathbf{s}_k, \mathbf{s}_{k+1}, \mathbf{a}_k, \mathbf{r}_k)\}$
- 7 **if** $L_{\text{model}}(D_{\text{val}}) < \text{tol}$ **then**
// agent-model interaction
- 8 Sample uniformly a batch of initial states $\{\mathbf{s}_k\} \sim \mathcal{D}_{\mathcal{E}}, k \leftarrow 0$
- 9 **for** k' in $\{1, \dots, b\}$ **do**
10 Execute $\mathbf{a}_{k'} \leftarrow \pi_{\theta}(\cdot | \mathbf{s}_{k'})$ and observe $\mathbf{s}_{k'+1}, \mathbf{r}_{k'} \leftarrow \mathbf{M}_{\zeta}(\mathbf{s}_{k'}, \mathbf{a}_{k'})$ ▷ b -length model rollout
11 Store $\mathcal{D}_{\mathbf{M}_{\zeta}} \leftarrow \mathcal{D}_{\mathbf{M}_{\zeta}} \cup \{(\mathbf{s}_{k'}, \mathbf{s}_{k'+1}, \mathbf{a}_{k'}, \mathbf{r}_{k'})\}$
12 $k' \leftarrow k' + 1$,
- 13 Train policy by minimizing $J'(\pi_{\theta})$ in Eq. (22) using $\mathcal{D}_{\mathbf{M}_{\zeta}} \cup \mathcal{D}_{\mathcal{E}}$

to path $\phi_0^{(C)}$, then paths $\phi_t^{(A)}, \phi_t^{(B)}$ remain close compared to path $\phi_t^{(C)}$.

Both properties are well known [50,51] for ODEs and become very useful when we try to predict the trajectories from noisy quantum data by imposing strong priors on the space of learnable Hamiltonians. Property (b) is a consequence of Gronwall's inequality [51] and essentially can be interpreted as follows: ODE flows that start off closer (with respect to the initial condition) stay closer (with respect to the final condition). Both (a) and (b) essentially imply a sort of intrinsic robustness of the ODE flow $\phi_t(\mathbf{z}_0)$ to perturbations on \mathbf{z}_0 [32]. They constrain the trajectories predicted by the model \mathbf{M}_{ζ} to be intrinsically robust (over a finite time interval) to small noise in the states \mathbf{s}_k and inaccuracies in the learned system Hamiltonian $H_0^{(L)}(\zeta)$.

We call the SAC equipped with this differentiable ODE model the learnable Hamiltonian model-based SAC (LH-MBSAC) as listed in Algorithm 2. Crucially, LH-MBSAC generalizes the SAC by allowing the policy to interact with the ODE model and the physical system. LH-MBSAC gracefully falls back to the model-free SAC in the absence of a model with low prediction error that is measured from the performance of the model's predictions on an unseen validation set of interaction data. The threshold or tolerance level for switching to the agent-model interaction part of the algorithm is likely problem-dependent and thus needs to be selected along with other hyperparameters in RL. However, this allows us to improve the sample complexity of model-free reinforcement learning, when possible, by leveraging knowledge about the controllable quantum system, yet we are still able to control the system in a model-free manner if this is not possible.

IV. EXPERIMENTS

We demonstrate the performance of LH-MBSAC on three quantum systems of current interest in open and closed settings with shot noise. Measurements in this section are made using Pauli instead of the generalized Gell-Mann operators mentioned in Sec. II B, and the simulated systems are all qubit systems.

To warm up, the first system $\tilde{H}_{\text{NV}}^{(1)}$ is a single-qubit NV center with microwave pulse control [52],

$$\frac{H_{\text{NV}}^{(1)}(t)}{\hbar} = 2\pi \Delta \sigma_z + \underbrace{2\pi \Omega [u_1(t) \sigma_x + u_2(t) \sigma_y]}_{H_c(t)}, \quad (25)$$

where $\Delta = 1$ MHz is the microwave frequency detuning, $\Omega = 1.4$ MHz is the Rabi frequency, and the control field parameters are $u_j(t)$ in the range $\mathbb{X}_{\text{NV}}^{(1)} = \{-1 \leq u_j \leq 1\}$. In this and subsequent examples, terms not covered by $H_c(t)$ are learned, parametrized by the learnable model parameters ζ . The gate operation time is 20 μs .

The second system $H_{\text{NV}}^{(2)}$ is a two-qubit NV center system [35], driven by microwave pulses of approximately 0.5 MHz, modeled as follows:

$$\begin{aligned} \frac{H_{\text{NV}}^{(2)}(t)}{\hbar} = & |1\rangle\langle 1| \otimes [-(v_z + a_{zz})\sigma_z - a_{zx}\sigma_x] \\ & + |0\rangle\langle 0| \otimes v_z \sigma_z + \underbrace{\sum_{l=x,y} \sum_{k=1}^2 \sigma_k^{(l)} u_{lk}(t)}_{H_c(t)}, \quad (26) \end{aligned}$$

where $v_z = 0.158$ MHz, $a_{zz} = -0.152$ MHz, and $a_{zx} = -0.11$ MHz, $\sigma_k^{(l)}$ is the l th Pauli operator on qubit k , and $u_{lk}(t)$ is a time-dependent control field. The range of control is $\mathbb{X}_{\text{NV}}^{(2)} = \{-1 \text{ MHz} \leq u_{lk} \leq 1 \text{ MHz}\}$ and the final gate time is $T = 2 \mu\text{s}$.

The third system $\tilde{H}_{\text{tra}}^{(L)}$ is an effective Hamiltonian model for cavity quantum electrodynamics (cQED) [36] for two transmons or qubits as a proxy for the IBM quantum circuits [53],

$$\begin{aligned} \frac{H_{\text{tra}}^{(2)}(t)}{\hbar} &= \sum_{l=1}^2 \omega_l \hat{b}_l^\dagger \hat{b}_l + \frac{\eta_l}{2} \hat{b}_l^\dagger \hat{b}_l (\hat{b}_l^\dagger \hat{b}_l - 1) \\ &+ J \sum_{l=1}^2 (\hat{b}_l^\dagger \hat{b}_{l+1} + \hat{b}_l \hat{b}_{l+1}^\dagger) + \underbrace{\sum_{l=1}^2 u_l(t) (\hat{b}_l + \hat{b}_l^\dagger)}_{H_c(t)}. \end{aligned} \tag{27}$$

This model consists of Duffing oscillators with frequency $\omega_l = 5$ GHz representing the qubits with an anharmonicity $\eta_l = 0.2$ GHz, qubit coupling J , and a control field u_l per qubit. This is a special case of the Bose-Hubbard model [54], with \hat{b}_l representing the boson annihilation operator on the j th qubit. The control field $u_l(t)$ is real by construction in addition to extra constraints imposed on the space of possible controls \mathbb{X} . The range of control is given by $\mathbb{X}_{\text{tra}}^{(2)} = \{-0.2 \text{ GHz} \leq u_l \leq 0.2 \text{ GHz}\}$ and the final gate time is $T = 20 \mu\text{s}$.

For the two-qubit system the target gate is CNOT, and for the one-qubit system it is the Hadamard gate. Pulses are discretized in accordance with the scheme introduced in Sec. II C for the number of time steps, $N = 20$. We follow the parameter restrictions for all systems introduced in Refs. [10,35,36,52]. Moreover, due to limited support in our autodifferentiation library [55], we simulate the complex dynamics by mapping the complex ODE to two real coupled ODEs [20] (see Appendix A for more details on our ODE solver).

The following sections are organized as follows. In Sec. IV A, we demonstrate a sample complexity improvement for the different control problems discussed above in a noisy closed setting. For the subsequent sections, we study the two-qubit transmon control problem in more detail. The results were similar for other systems that we studied. In Sec. IV B, we study the effect of increasing the estimated Hamiltonian error from its true value on the sample complexity of control. Section IV C discusses how the learned Hamiltonian in LH-MBSAC can be further utilized for model-based control using gradient-based methods like GRAPE. Section IV D extends results from the closed setting to the noisy open system setting. Finally, in Sec. IV E, we highlight some limitations and silver linings of the LH-MBSAC and the RL-for-control approach for our specific MDP [Eq. (17)] in this paper and provide promising ideas to circumvent some of the issues.

A. Sample efficiency for closed system control

In this section, we only consider closed or unitary system control with and without single-shot measurements defined in Sec. II A. From here on, we refer to single-shot measurements as just “shots.”

Unitary control (with closed system dynamics) is implemented for shots as a special case of open system control where the dissipation operator \mathcal{L} is 0. The Choi operator Φ corresponding to the gate realized by the controls is obtained by sampling from the binomial distribution in Eq. (12) with $M = 10^6$ shots per measurement operator. By Hoeffding’s inequality [56], we know that with probability $1 - 0.01$ the error in the estimator of q_l is 10^{-3} . Or generally, with probability $1 - \delta$, for ϵ error, we require $O(\log \frac{1}{\delta} / \epsilon^2)$ measurements. The AAPT method [45] (see Sec. II B) uses $M \times 3^L$ shots in total for 3^L possible measurement operators for an L -qubit system, which is quite expensive.

Further sparsity restrictions on the structure of Φ imposed by a k -local Hamiltonian, where qubit interactions up to only the nearest $k \leq L$ qubits are assumed, can allow the shot cost to go down to $O(4^k (\log M) / \epsilon^2)$ for M observables due to a reduction in the number of observables that need to be measured or tracked, which is asymptotically optimal in the number of measurements [57]. However, since the goal of this paper is gate control, these costs are generally unavoidable to completely verify gate performance. In practice, such gates are only limited to a few qubits, and operations on many qubits are achieved in the circuit formalism through gate composition [53,58].

We randomly initialize the learnable system Hamiltonian using the Pauli basis parametrization in Eq. (23) with coefficients $\zeta_i \sim \text{Uniform}(-1, 1)$. The environment’s data buffer $D_\mathcal{E}$ that stores the model’s training data, i.e., the initial exploration data set (see Algorithm 2), consists of 1, 20, and 100 pulse sequences for the one-qubit NV, two-qubit NV, and two-qubit transmon systems, respectively. A more detailed discussion of the amount of training data needed for Hamiltonian learning is presented in Appendix D. These data are collected using random uniform policy actions during the first run of the LH-MBSAC algorithm.

The exploration data set is then used to learn the system Hamiltonians $H_{\text{0NV}}^{(1)}$, $H_{\text{0NV}}^{(2)F}$, $H_{\text{0tra}}^{(2)}$ via supervised learning of \mathbf{M}_ζ using the dynamics prediction loss function [Eq. (24)] until a validation loss of around $10^{-3} \times 2^{2q} \times \text{batch_size}$ is reached, where `batch_size` is the number of samples used for a single training policy update. Here q is the number of qubits and $q = 2$ for the theoretical unitary and $q = 4$ for the Choi state (due to the Choi-Jamiolkowski isomorphism in AAPT).

After this, we switch to the model \mathbf{M}_ζ to generate synthetic samples to train the policy π . While concurrently maintaining policy interactions and attempting control of the system via the policy π , the model is successively trained in periods with fresh data to reduce the model error even further. Once the policy starts producing pulses with nearly optimal fidelities of around 0.98, we terminate the algorithm and use the learned Hamiltonian to further optimize the pulses using gradient-based methods like GRAPE to (a) reduce sample complexity costs and (b) improve runtime of LH-MBSAC, since the model simulations are computationally expensive. We found that terminating around 0.98 ensures that the application of further gradient-based methods does not cause the control parameters to diverge too much from their initial values, thereby retaining, at least partially, their favorable

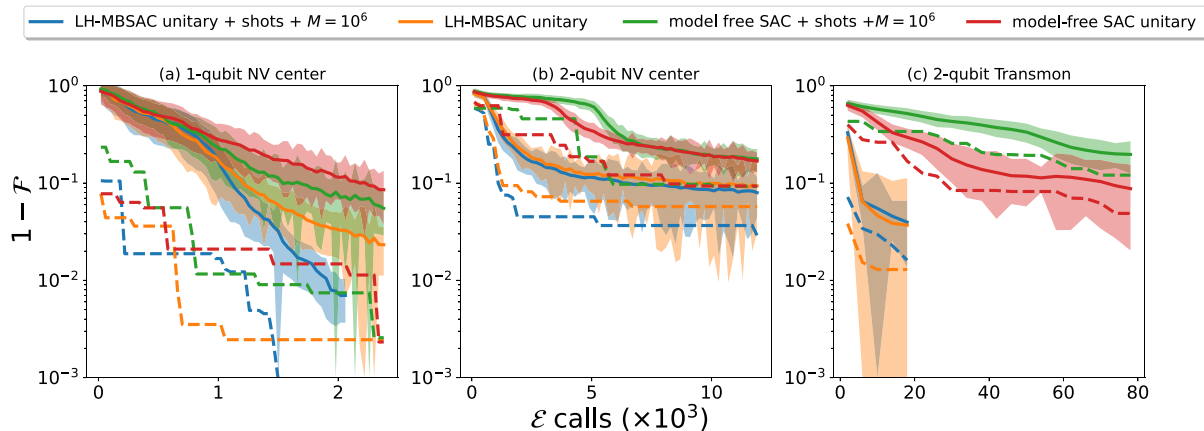


FIG. 2. The closed system fidelity \mathcal{F} of the Hadamard gate for (a) $H_{NV}^{(1)}$, and of the CNOT gate for (b) $H_{NV}^{(2)}$ and (c) $H_{tra}^{(2)}$ as a function of the number of environment \mathcal{E} calls. The mean fidelity over 100 controllers is plotted as a solid line with the shading indicating two standard deviations, and the maximum fidelity is indicated by the dashed line. LH-MBSAC or model-free SAC with the unitary tag indicates the shot-noise-free closed system problem in Eq. (4), and single-shot measurements are likewise indicated. We terminate the algorithm early at $\mathcal{F} > 0.98$ for LH-MBSAC with and without single-shot measurements since the model simulations are expensive and the learned model at this point can be used to further optimize the moderately high fidelity RL pulses further, as shown in Sec. IV C. The sample complexity of LH-MBSAC is significantly improved for the two-qubit transmon and the NV center over model-free SAC for the closed system control problem and with single-shot measurements (of size $M = 10^6$), using AAPT. We average these results over three seeds of each algorithm run where a seed refers to a single algorithm run from scratch with a fresh set of randomly initialized parameters.

robustness properties [12]. Step (b) is discussed in detail in Sec. IV C.

The results for LH-MBSAC and model-free SAC for the one- and two-qubit control problems are shown in Fig. 2. We consider LH-MBSAC’s performance with shots by estimating the gate using its corresponding estimated Choi state Φ using AAPT with 10^6 shots per observable. The sample complexity of LH-MBSAC to achieve a maximum fidelity significantly improves, by at least an order of magnitude, upon the model-free baseline in both cases, although it is more significant for the two-qubit transmon.

B. Sample complexity as a function of Hamiltonian error

Continuing with the closed system control problem, in this section we study the relationship between sample complexity and error in the estimated model Hamiltonian $H_0(\xi)$ compared to the true system Hamiltonian H_0 as the error is increased. This relationship is highly nonlinear or irregular and is discussed in detail later in the section. On a high level, the purpose of this section is to understand the interplay between control and model learning especially if the model is inaccurate. Can we still learn a near-optimal control policy even if the model is incorrect? To an extent, yes: we show that when the model error is small, LH-MBSAC is able to successfully find a near-optimal control pulse, even with an incorrect model.

We define the model error δ as in Ref. [59]:

$$\delta = \|H_0(\xi) - H_0\|, \tag{28}$$

where $\|\cdot\|$ is the spectral norm (the largest singular value) of $H_0(\xi) - H_0$. For this study, we compare two settings for some value of δ in each experimental run: (i) *learning the system Hamiltonian*, i.e., δ is decreased from its initial value; (ii) *not learning the system Hamiltonian*, i.e., δ remains fixed

throughout the experiment. Case (ii) effectively corresponds to Algorithm 2 without any model training, i.e., we do not attempt to minimize $L_{\text{model}}(D_{\text{train}})$ to update the model and instead set the model to have a fixed constant Hamiltonian error δ . The range of Hamiltonians corresponding to different δ values is chosen by randomly sampling the true Hamiltonian with rejection using Gaussian perturbations. The nonlinear dependence on the sample complexity of LH-MBSAC as a function of δ for the two-qubit transmon control problem for both cases is shown in Figs. 3(a)–3(e) for $\delta \in \{0.01, 0.02, 0.05, 0.1, 0.2\}$.

For the two-qubit transmon problem, the $\delta = 0.02, 0.05, 0.1$ results show worse performance compared to the $\delta = 0.2$ results for the theoretical unitary control problem (without measurement noise). This indicates that some model system Hamiltonians $H_0(\xi)$ with a larger δ predict dynamics more consistent with the true system Hamiltonian H_0 dynamics than $H_0(\xi)$ with a smaller δ . However, learning $H_{0\text{tra}}^{(2)}$ for all shown cases restores performance for both the noiseless unitary and shots-based closed system control problems.

To explain these empirical results and make them more intuitive, we now make use of the integration by parts lemma of Ref. [59] that bounds δ by the unitary prediction error of the ODE model with respect to the environment for the unitary control problem Eq. (4).

Proposition 1. The following bound holds for the difference between the unitary model’s predicted state U_{M_ξ} and the environment’s unitary state $U_\mathcal{E}$,

$$\|U_\mathcal{E} - U_{M_\xi}\|_{\infty,t} \leq t^2 \delta \left(\frac{1}{t} + \frac{2}{t} \|H_c\|_{1,t} + \|H_\xi\| + \|H_\mathcal{E}\| \right), \tag{29}$$

where $\|\cdot\|$ is the spectral norm, and for some linear operator A we have $\|A\|_{\infty,t} = \sup_{s \in [0,t]} \|A(s)\|$ and $\|A\|_{1,t} = \int_0^t ds \|A(s)\|$.

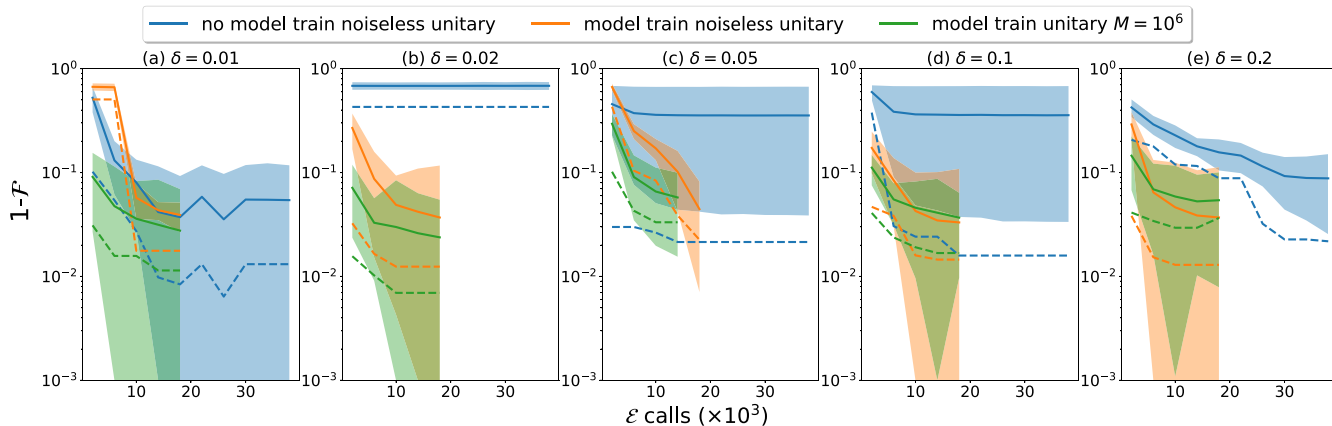


FIG. 3. Sample complexity or \mathcal{E} calls of LH-MBSAC for the two-qubit transmon control problem as a function of spectral norm error δ , quantifying the closeness of the learned system Hamiltonian $H_0(\zeta)$ and the true system Hamiltonian H_0 . The cases for $\delta = 0.01, 0.02, 0.05, 0.1, 0.2$ are plotted in (a)–(e). The mean fidelity over 100 controllers is plotted as a solid line, with the shading indicating two standard deviations, and the maximum fidelity is indicated by the dashed line. The “noiseless unitary” is the no shot noise setting where the exact unitary is seen by the algorithm while alternatively the unitary is estimated using AAPT with $M = 10^6$ shots per observable characterizing the Choi state. The “no model train” line indicates the setting where no learning of $H_0(\zeta)$ occurs and δ is fixed while the “model train” lines denote the setting where δ is reduced through model training. In general, we see that there are some instances where the RL agent is able to optimize the objectively wrong model $\delta = 0.2, 0.01$, and there is a nonlinear dependence of \mathcal{E} calls on δ , i.e., a large δ can produce better model-predictive trajectories with a smaller unitary prediction error. This points us to considering the idea of learning Hamiltonians that are only “locally consistent.” Once learning $H_0(\zeta)$ is enabled, algorithmic performance is restored in both the noiseless (with no shot noise) and shot-noise unitary settings. The number of measurements is $M = 10^6$ per observable.

Proof. See the proof of Proposition 2 in Appendix B. ■

Proposition 1 hints at the intuition for why the Hamiltonian error is generally not linearly related to the propagator error.

Although there are some works with better relational bounds on the Hamiltonian error in terms of the observable error, these hinge on the ability to maintain a privileged basis and/or access to special probe states such as the Gibbs state basis [60,61]. These bounds crucially do not include the propagator error, thanks to previous assumptions, which is a more general approach to bounding the quantum dynamical evolution error. Of course, there is always a price to be paid for generality, and in this case it is that the error bounds are less constrained and the link between the Hamiltonian and the unitary error becomes nonlinear for the general case of the bound.

From Proposition 1, we infer that the unitary model prediction error or the supervised learning regression loss $L_{\text{model}}(D_{\text{train}})$ in Eq. (24) being small does not imply closeness between learned and true system Hamiltonian, i.e., $\delta \rightarrow 0$. However, in the converse case, δ being very small necessarily implies small propagator error. This is illustrated for the two-qubit transmon Hamiltonian in Fig. 4(a). The Hamiltonians are again sampled using Gaussian perturbations to the transmon Hamiltonian. There is also significant variation in the unitary model prediction error, even for the same value of δ for different repetitions of the random Hamiltonian. However, we see that with decreasing δ , the variation decreases, which is also explained by the above bound. Finally, the same pattern can also be observed if we take δ to be the mean-squared difference between the Pauli

coefficients of the true and learned Hamiltonian. Thus, this behavior is general and not limited to the choice of δ .

The main takeaway of this section, that will be addressed further in the next section, is that for the control problems considered here, it is only necessary to learn models that are “locally consistent” in terms of the unitary trajectories they generate, and small unitary prediction errors can be achieved by models with non-negligibly small δ .

C. Leveraging the learned Hamiltonian with GRAPE

Proposition 1 paves the way for learning system Hamiltonians that are locally consistent with the unitary trajectories they generate. By local, we mean that the learned Hamiltonian is consistent with the true Hamiltonian on only a subset of all possible generatable trajectories relevant to the control problem. In this section, we delve deeper into the learned model errors and also show that these local models can be leveraged to further optimize the fidelities of LH-MBSAC’s controllers using gradient-based methods like GRAPE [7,9].

During the model’s \mathbf{M}_ζ training phase, $H_0(\zeta)$ is made consistent with trajectories uniform randomly drawn from the data buffer $D_\mathcal{E}$ by minimizing the regression loss $L_{\text{model}}(D_\mathcal{E})$. This allows us to learn a model of the environment that can predict locally consistent unitary trajectories (i.e., at the scale of the control problem). In other words, the learned system Hamiltonian $H_0(\zeta)$ does not have to coincide with the true system Hamiltonian H_0 for it to be useful for the optimal control task. Indeed, we take the Hamiltonian learned for the two-qubit transmon in Fig. 2(c) and find that it has $\delta = 0.91509$. Diving deeper, the matrix difference between the true H_0 and

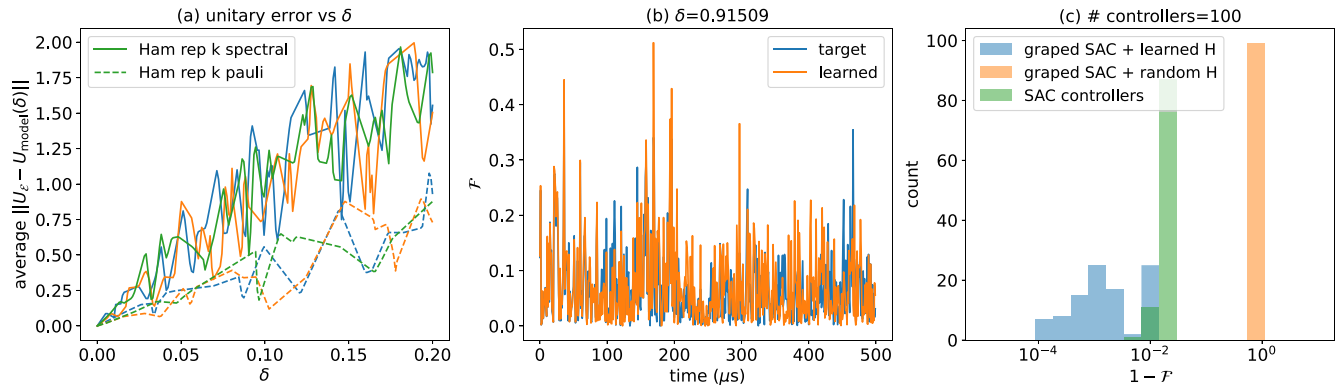


FIG. 4. (a) An illustration of the nonlinear relationship between the unitary model prediction error $\|U_\xi - U_{\mathbf{M}_\xi}\|$ and the Hamiltonian spectral norm (solid) error or mean-squared Pauli basis difference (dashed) error as δ for the two-qubit transmon control problem. For the same 1000 random control pulses, we evaluate the average unitary prediction error of \mathbf{M}_ξ with increasing δ for three different uniform randomly sampled two-qubit Hamiltonians $H_0(\xi)$ to illustrate the variation in response to the unitary error. (b) Local and global unitary trajectories: \mathcal{F} as a function of a random control pulse with either the learned system Hamiltonian $H_0(\xi)$ or the true system Hamiltonian H_0 . The learned $H_0(\xi)$ trajectories do not coincide with the global trajectory with $\delta = 0.91509$, with the majority contribution coming from a global phase factor such that $\text{Tr}[H - H_0(\xi)] \approx 0.9$. Both trajectories start off extremely close and start diverging as time increases due to accumulation of small errors in the predicted dynamics. (c) The learned $H_0(\xi)$ can be leveraged using GRAPE to further optimize the fidelities of LH-MBSAC's controllers. We plot a histogram of 100 LH-MBSAC controller infidelities $1 - \mathcal{F}$ before and after applying GRAPE on these controllers using the learned Hamiltonian and a random Hamiltonian. The LH-MBSAC fidelities are significantly improved after applying GRAPE. The appropriate baseline or benchmark representing our ignorance of H_0 is a random $H_0(\xi)$ (with uniform random Pauli parameters), which, when plugged into GRAPE, yields extremely low fidelities near 0 towards the extreme right-hand side of the plot.

learned Hamiltonian $H_0(\xi)$ is

$$H - H_0(\xi) = \begin{bmatrix} -0.912 & 0.001 & -0.001 & 0.001 \\ 0.001 & -0.914 & 0.001 - 0.001i & 0.001 + 0.001i \\ -0.001 & 0.001 + 0.001i & -0.913 & -0.001 \\ 0.001 & -0.001 - 0.001i & -0.001 & -0.914 \end{bmatrix}.$$

Notably, we can see that most of the error is actually in $\text{Tr}[H - H_0(\xi)]$ with the true Hamiltonian being learned up to a scale factor of around 0.9 with the rest of the parameter error being small. This is precisely the global phase error that cannot be learned [62].

Despite this discrepancy between the true and learned system Hamiltonians, we find mostly good local agreement between the two random trajectories that they induce thanks to the supervised training phase of the model. We show in Fig. 4(b) the local and global trajectories corresponding to $H_0(\xi)$ and H_0 for the two-qubit transmon, which shows that the two unitary trajectories with respect to the CNOT fidelity are not always coinciding. More specifically, we can see a high overlap in the fidelities induced by random pulses for times from $0 \mu\text{s}$ to around $100 \mu\text{s}$. Moreover, the small differences in the generator only start manifesting as the timescales get longer, and this can be explained by accruing small errors in predicted dynamics. This confirms that the unitary model prediction error grows as a function of time. This makes intuitive sense since predictions far into the future, compared to their timewise preceding counterparts, must necessarily have more built-up error. Furthermore, this learned “local” $H_0(\xi)$ and the controllers found by LH-MBSAC can be used in conjunction with the model-based GRAPE control algorithm [7,9] to optimize the SAC controller fidelities much more quickly than via just RL alone using accelerated second-order

gradient descent. The LH-MBSAC controllers act as seeds, so GRAPE does not move too far away in pulse parameter space compared to where it started. Although not done here, this can also be imposed as an explicit constraint. Note that the question of exactly when to switch over to GRAPE beyond heuristics remains unanswered.

The fidelities after applying GRAPE are evaluated with respect to the true system Hamiltonian H_0 . Usually LH-MBSAC controllers have moderately high fidelities around $\mathcal{F} > 0.98$ which are improved to $\mathcal{F} > 0.999$. In Fig. 4(c), we show the RL controllers being optimized further using the learned $H_0(\xi)$ with GRAPE. Experiments in this section for the two-qubit NV center system yield similar results and can be found in Appendix E.

D. Open system control with single-shot measurements

Due to the interpretable nature of our ODE model's ansatz in Eq. (23), it is pertinent to ask if two competing but linear terms in the model \mathbf{M}_ξ can be learned simultaneously. In this section, we find that for our model learning setting, the answer to this question is no. However, this is not general to all problem settings and could potentially be pursued in future work.

In the previous sections, we only learn one term represented by $H_0(\xi)$. Utilizing the open system formulation of

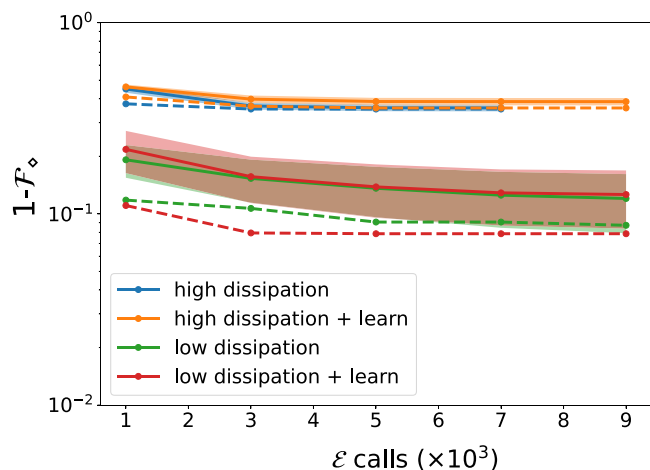


FIG. 5. Diamond norm fidelity \mathcal{F}_\diamond for the two-qubit transmon control problem in low and high Lindblad dissipation regimes for LH-MBSAC. The results are averaged over two seeds with the mean \mathcal{F}_\diamond over 100 controllers shown by solid lines and the maximum \mathcal{F}_\diamond by dashed lines. Shading denotes two standard deviations from the mean. Here, the “learn” label signifies that dissipation operators are being learned in addition to the system Hamiltonian.

the control problem in Sec. II B, we consider Lindblad dissipation along with shot noise for the two-qubit transmon control problem in Eq. (14). Specifically, we consider the decoherence operator $\mathcal{L}_{\text{diss}}^{(l)} = \sqrt{\frac{2}{R_l^*}} b_l b_l^\dagger$, acting on the l th qubit, and the decay operator $\mathcal{L}_{\text{decay}}^{(l)} = \sqrt{\frac{2}{R_l}} b_l$ for $l = 1, 2$. R_l^* and R_l are the decoherence and decay rates. Both operators are time-independent

Alternatively, we can also represent these operators using the adjoint representation, but we note that in the context of this learning problem that representation will not make much difference as our algorithm is able to effectively learn the Hamiltonian up to the addition of a scalar matrix. However, practically speaking, one can obtain the energy differences of the Hamiltonian via spectroscopy [63], which can then be encoded in the eigenvalues of the adjoint representation. It is also possible to learn these eigenvalues using measurements of canonical (Gibbs) states [60].

We perform experiments for high and low dissipation corresponding to the gate times $R_l^{*hi} = R_l^{hi} = 4 \mu\text{s}$ and $R_l^{*lo} = R_l^{lo} = 20 \mu\text{s}$. Comprising both of these time-independent operators, the Lindblad term \mathbf{L}_1 is learned concomitantly with the system Hamiltonian. The results are shown in Fig. 5, where the “learn” label signifies that \mathbf{L}_1 is being learned in addition to the system Hamiltonian $H_0(\xi)$.

We use the diamond norm fidelity [64] \mathcal{F}_\diamond ,

$$\mathcal{F}_\diamond(\Phi(\mathbf{u}(t), t), \Phi_{\text{target}}) = 1 - \|\Phi(\mathbf{u}(t), t) - \Phi_{\text{target}}\|_\diamond, \quad (30)$$

instead of the generalized state fidelity since the latter lacks the sensitivity to detect the low dissipation regime (see Appendix G). We find that attempting to learn \mathbf{L}_1 while learning $H_0(\xi)$ confers little to no advantage in both the high and low dissipation regimes for this control task. Further investigation shows that the estimate of the system Hamiltonian $H_0(\xi)$ compensates for the observed discrepancy in observed

dynamics due to dissipation as much as it is unitarily possible. Moreover, the learning processes for \mathbf{L}_1 and $H_0(\xi)$ become entangled/mixed, so learning multiple independent terms in \mathbf{M}_ξ may not be suitable for LH-MBSAC.

E. Limitations and silver linings

There are two major limitations of LH-MBSAC. The first is that only the system or time-independent part of the Hamiltonian can be learned with the algorithm, while the more difficult problem of learning the time-dependent part of the Hamiltonian [62] is left as future work.

Moreover, we found that LH-MBSAC was not able to tackle a three-qubit transmon control problem to obtain a Toffoli gate on an extension of the transmon system. The limitation applied mostly to the RL agent; a viable Hamiltonian is learned that can be leveraged with GRAPE as before. Specific computational details are discussed in Appendix F. Essentially, our findings indicate this is an optimization landscape problem and an issue specific to the meta RL strategy of finding optimal pulses instead of a hyperparameter problem. There are two major reasons behind this assessment. First, the values and the gradients for policy and value functions saturate with large training times, i.e., both are stuck in suboptimal extrema, which ultimately culminate with a prematurely optimized reward function. Secondly, since the model Hamiltonian is known beforehand (or also learned), GRAPE equipped with this Hamiltonian and initialized with the highest fidelity LH-MBSAC controllers also gets stuck.

However, the LH-MBSAC strategy is not limited to SAC and can augment different RL algorithms for which the three-qubit problem may be tractable. Also, since this is likely an optimization landscape issue, a reformulation of the RL control problem could also alleviate this issue by reducing the probability of SAC getting stuck by increasing the range of fidelities the RL agent sees as “proximally optimal.” At present, the agent’s goal is to maximize all fidelities it observes, with most of the observations being premature, i.e., before the final gate time. This is highlighted in Fig. 6, which shows the infidelity $1 - \mathcal{F}$ as a function of time for 100 pulses found by LH-MBSAC and GRAPE for the two-qubit transmon control problem. Compared to GRAPE, LH-MBSAC pulses are much more consistent and periodic in terms of the intermediate fidelity values. This highlights that the RL approach is biased towards optimizing intermediate fidelities along with the final target fidelity [since the objective function in Eq. (19) is the regularized expected cumulative fidelity]. This is quite different from the approach taken by the gradient-based GRAPE algorithm. Despite being interesting from a controller robustness point of view [12], this bias can prevent solutions that do not admit high intermediate fidelities from being found as RL can get stuck in a loop mining medium-level fidelity values. Stepping away from this particular sequential decision-making MDP formulation might be one solution to consider in future work.

There are silver linings for the aforementioned MDP formulation. RL pulses are fidelity-wise better, on average, across the duration of the pulse. Leveraging the learned system Hamiltonian, we can further improve the performance of the RL pulses by using GRAPE with the RL pulse

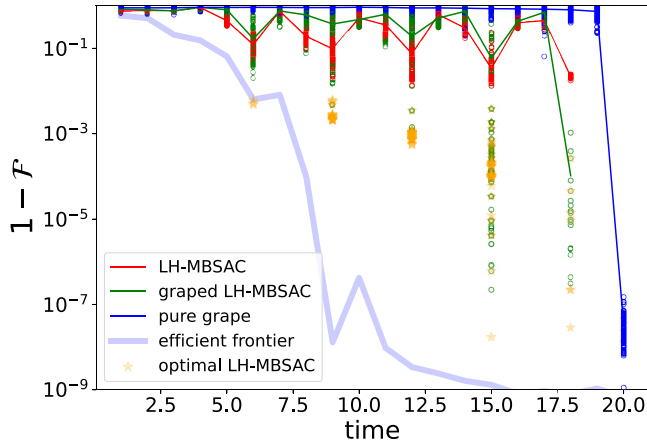


FIG. 6. The infidelities over time for 100 different control pulses found by LH-MBSAC and by GRAPE using the learned system Hamiltonian $H_0(\xi)$ for the two-qubit transmon control problem with final time $T \leq 20 \mu\text{s}$. RL pulses are further optimized using GRAPE. GRAPE is also used to obtain pulses without the RL controls as initial values for a fixed final gate time $T = 20 \mu\text{s}$. Short optimal controls found by RL are identified by truncating RL pulse parameters at times $t \geq \{6, 9\} \mu\text{s}$ whose final infidelities are shown as stars, with $t = 6 \mu\text{s}$ being Pareto optimal with respect to the efficient frontier (the surface indicating the best fidelity for that time).

parameters as initialization. As seen in Fig. 6, these pulses are still better than the ones found by GRAPE using the learned system Hamiltonian but with completely random pulse initializations, i.e., without LH-MBSAC controllers as seeds.

Furthermore, this RL bias towards valuing intermediate fidelities allows us to identify optimal pulses that can be executed in short times, which is a difficult problem for GRAPE even if the final gate time is explicitly added to the control objective [9].

Truncating the control sequence for pulses at time t if the infidelity is below 5×10^{-2} , we again leverage GRAPE to maximize the final fidelities at these shorter times. These are shown as stars in Fig. 6 with the fidelities at $t = 6 \mu\text{s}$ being approximately Pareto optimal, i.e., the best fidelity for that time. The Pareto optimal efficient frontier is constructed by sampling 100 GRAPE pulses with random initializations at different final gate times.

V. CONCLUSION

We have presented a learnable Hamiltonian soft actor-critic (LH-MBSAC) algorithm for time-dependent noisy quantum gate control. LH-MBSAC augments the model-free soft-actor critic by allowing the reinforcement learning (RL) policy to query a learnable model of the environment or the controllable system. It thereby reduces the total number of queries (sample complexity) required to solve the RL task. The model is a differentiable ODE with a partially characterized Hamiltonian, where only the parametrized time-independent system Hamiltonian is required to be learned. This is a good inductive bias for the quantum control task as ODE trajectories do not intersect, and the Schrödinger ordinary differential equation (ODE) preserves unitary evolution, thereby sensibly constraining the space of models to be learned. Using

exploration data acquired from the policy during the RL loop, we train the model by reducing a model prediction error over the data. We show that LH-MBSAC is able to reduce the sample complexity for gate control of one- and two-qubit nitrogen-vacancy (NV) centers and transmon systems in unitary and single-shot measurement settings.

Moreover, we highlight that despite the generally nonlinear relationship between the error in the learned Hamiltonian and the model prediction error, LH-MBSAC's performance is robust to this variation. Furthermore, even if the learned Hamiltonian that minimizes the model prediction error is not the same as the true system Hamiltonian, the learned Hamiltonian which is locally consistent in terms of its dynamical predictions can be leveraged using gradient-based methods that require full knowledge of the controllable system, like GRAPE, to further optimize the controllers found by LH-MBSAC. Applying LH-MBSAC in high and low Lindblad dissipation regimes with shot noise, we found that its performance in both was not improved if the Lindblad dissipation terms are also learned in addition to the system Hamiltonian as it is likely that the latter part compensates for the extra dissipation effects.

Despite LH-MBSAC's limitations requiring it to know the time-dependent Hamiltonian and system scalability beyond two qubits [four with single-shot measurements due to ancilla assisted process tomography (AAPT)], the algorithm can be used to augment many existing model-free RL approaches for quantum control. This should afford more sample-efficient RL-based optimization of quantum dynamics for near-term noisy quantum processors on a variety of architectures, as shown in the paper. Specific tasks can include noisy small circuit optimization, state preparation [14,15], or gate optimization using a partially known model of the underlying dynamics [13]. Since having an accurate model can be extremely useful for validation of quantum operations, and because model bias can be crippling, model-based RL methods like LH-MBSAC can improve the model specifically tailored for some downstream task, e.g., quality assessment of topological codes [65] or fine-tuning current implementations of a two-qubit cross resonance gate on some novel architecture [24] using a preexisting but partially correct model. Here, the goal for the RL agent would be to help learn effective and potentially scalable models of the target system while optimizing the target functional. Another interesting goal in this direction could just be incorporating the number of measurements or queries of the system in the RL objective so that the learning is sample-efficient. Another avenue of future work is to combine LH-MBSAC with a more feasible measurement protocol than AAPT. AAPT is not a hard requirement for our approach, and it was used here for its theoretically simple estimation of a quantum process. Two angles of attack are either sparsity assumptions on the dynamics generator [66] and the generated evolution [57], or a partially observed Markov decision process formulation of the control problem [6,67].

Moreover, despite the scalability problems due to the potentially hindering nature of the RL strategy towards maximizing intermediate fidelities, it can be useful in particular to identify short time optimal pulses. Learning the time-dependent part of the Hamiltonian is harder and might require a stronger learning protocol, e.g., using the zero-order hold

method with the learning protocol presented in this paper, Bayesian Hamiltonian learning [62], or a more informative learning process or Hamiltonian learning methods [66,68] which would be exciting to pursue in the future.

The study of the abilities and limitations of our Hamiltonian learning protocol using ZOH will be left to future work. Our code is available at [69].

APPENDIX A: MAPPING COMPLEX LINEAR ODES TO COUPLED REAL ODES AND STEP-SIZE EFFECTS

The quantum control problem in Eqs. (4) and (14) involves ODEs [Eqs. (2) and (9)] in the complex domain with a complex vector field map $f_\theta : \mathbb{R} \times \mathbb{C}^d \rightarrow \mathbb{C}^d$ (where θ denotes some learnable parameters that can be optimized). For the unitary control problem, we have a linear map $f_\theta(U(\mathbf{u}(t), t), t) = H_\theta(\mathbf{u}(t), t)U(\mathbf{u}(t), t)$, where H_θ is a Hermitian Hamiltonian that generates the ODE path of the propagator $U(t)$. We make use of the following isomorphism to map the complex ODE to two coupled real ODEs in \mathbb{R}^{2d} by separating the propagator into its real and imaginary parts $U = U_{\text{real}} + iU_{\text{imag}}$ and mapping the Hamiltonian isomorphically, $H(\mathbf{u}(t), t) \rightsquigarrow \mathbb{1} \otimes H_{\text{real}}(\mathbf{u}(t), t) - i\sigma_y \otimes H_{\text{imag}}(\mathbf{u}(t), t)$, to get the following [20] coupled real ODE system:

$$\begin{aligned} \frac{d}{dt} \begin{pmatrix} U_{\text{real}}(\mathbf{u}(t), t) \\ U_{\text{imag}}(\mathbf{u}(t), t) \end{pmatrix} &= \begin{pmatrix} H_{\text{imag}}(\mathbf{u}(t), t) & H_{\text{real}}(\mathbf{u}(t), t) \\ -H_{\text{real}}(\mathbf{u}(t), t) & H_{\text{imag}}(\mathbf{u}(t), t) \end{pmatrix} \begin{pmatrix} U_{\text{real}}(\mathbf{u}(t), t) \\ U_{\text{imag}}(\mathbf{u}(t), t) \end{pmatrix}. \end{aligned} \tag{A1}$$

The mapping is analogous for the superoperator ODE in Eq. (9). Likewise, various other metrics, e.g., fidelity \mathcal{F} , were analogously transformed. We made use of the real nature of the Pauli vector decomposition of H to keep track of both the time-independent learnable Hamiltonian and the time-dependent control Hamiltonian representations.

We use Heun’s method [70] to implement a custom differentiable numerical ODE solver in `pytorch` [55], a popular automatic differentiation code library. The solver is able to evolve multiple ODEs under multiple generators in parallel using generalized matrix/tensor operations (ideally on a GPU to maximally leverage computational efficiency). The solver can be accessed in the `LearnableHamiltonian` module in our code [69]. To determine the optimal tradeoff between accuracy of dynamical simulation, computed gradients, and the size of the computation graph that is held in memory for automatic differentiation, we conduct experiments by simulating the dynamics of random n -qubit Hamiltonians from $n = 1$ to 4 at different precision or tolerance or step size of the ODE solver (see Fig. 7).

Computational speed of the solver naturally trades off with the accuracy in the simulation and the computed gradients. We find that a step size of 10^{-2} is sufficiently accurate for forward dynamical simulation (no gradients are computed in this step), and a step size of 5×10^{-4} is required for the backward step when the gradients need to be computed to train the ODE model. The errors in the dynamical predictions (averaged over many thousands of data points) in both steps are reasonably small and monitored. The ODE solvers in `scipy` [71] and the

matrix exponential method for solving linear ODEs [9] both have similar errors to those of our method for the step size 5×10^{-4} (likely the Bayes’ optimal error for our numerical simulation).

The ability to be fast but produce slightly less accurate predictions improved the wall time of our algorithm. Specifically, a significantly large number of trajectories can be quickly sampled in the forward step to augment the RL policy’s training data, while the much slower backward step can be limited to a smaller number of trajectories that need to be predicted and are divided over multiple batches.

APPENDIX B: BOUNDS ON THE MODEL PREDICTION ERROR

Consider a unitary RL control problem with the MDP in Eq. (17), where the environment’s Hamiltonian and propagator at some time step t_l are given by $H_\mathcal{E}(t_l, u_l) = H_0 + H_c(u_l, t_l)$ and $U_\mathcal{E}(\mathbf{u}_k)$. Now consider the model $\mathbf{M}_\zeta(\mathbf{s}_{k+1} | \mathbf{a}_k, \mathbf{s}_k)$ that predicts a single step of unitary dynamics $\mathbf{s}_k \xrightarrow{H_\zeta} \mathbf{s}_{k+1}$ under its parametrized generator $H_\zeta = H_0^{(L)}(\zeta) + H_c(u_l, t_l)$ following our assumptions in Sec. III. Now we bound the error in the single step predicted propagator U_ζ using the integration-by-parts lemma from Ref. [59]. We consider a continuous version of the propagators and the generators since the result is only used qualitatively.

Proposition 2 (Bound on the model predictions). The following bound between the unitary model’s predicted state $U_\zeta(\mathbf{u}_k)$ and the environment’s unitary state $U_\mathcal{E}(\mathbf{u}_k)$ holds:

$$\begin{aligned} \|U_\mathcal{E} - U_{\mathbf{M}_\zeta}\|_{\infty, t} &\leq t^2 \|H_0^{(L)}(\zeta) - H_0\| \cdot \left(\frac{1}{t} + \frac{2}{t} \|H_c\|_{1, t} + \|H_\zeta\| + \|H_\mathcal{E}\| \right). \end{aligned} \tag{B1}$$

Proof. The generator difference $H_\zeta - H_\mathcal{E} = H_0^{(L)}(\zeta) - H_0$ is time-independent. So the integral action difference term becomes

$$\begin{aligned} \left\| \int_0^t ds H_0^{(L)}(\zeta) - H_0 \right\|_{\infty, t} &= t \|H_0^{(L)}(\zeta) - H_0\|_{\infty, t} \\ &= t \|H_0^{(L)}(\zeta) - H_0\|, \end{aligned} \tag{B2}$$

where in the last line, we drop the supremum over time due to time independence. Now we can rewrite

$$\begin{aligned} \|H_\mathcal{E}(\mathbf{u}(t), t)\|_{1, t} &= t \|H_0 + H_c(\mathbf{u}(t), t)\|_{1, t} \\ &\leq t [\|H_0\| + \|H_c(\mathbf{u}(t), t)\|_{1, t}] \end{aligned} \tag{B3}$$

using the triangle inequality. Combining both facts yields the inequality. ■

The inequality in Eq. (B1) can be analogously extended to the open system setting with respect to the Choi matrix Φ . Here, we focus on the unitary case for simplicity since the arguments are similar.

There are two observations worth mentioning about inequality (B1): (a) when all other variables are fixed, the error in the model’s unitary predictions with respect to the environment’s ground truth grows as a function of time; (b) the model prediction error is a lower bound of the error in the

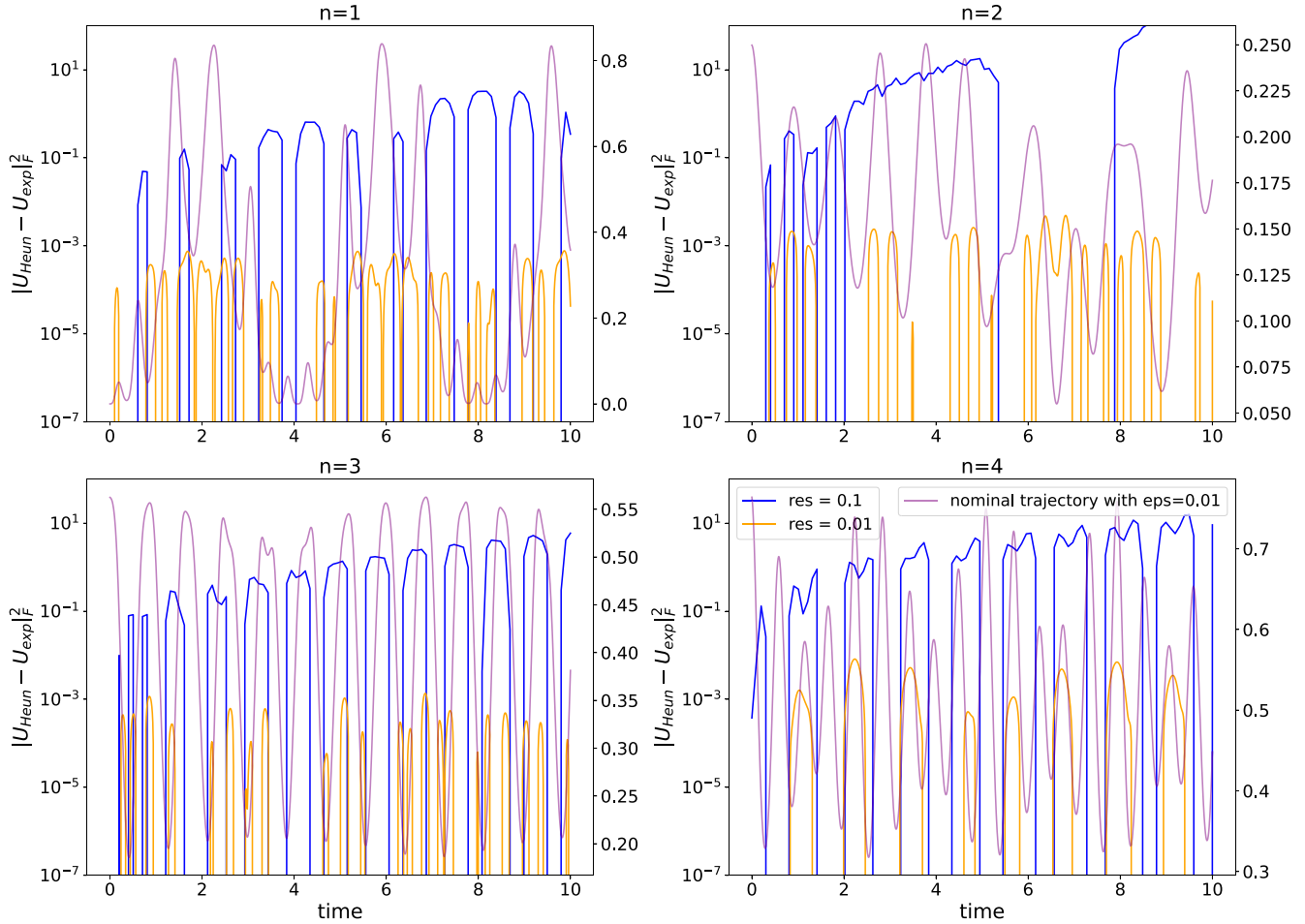


FIG. 7. Frobenius norm of the prediction error of the Heun ODE solver [70] compared to the matrix exponential method. The number of qubits n are shown on top of each subfigure. The random time-dependent sinusoidal Hamiltonians are as follows: for $n = 1$, $H = -2.32\sigma_z \cos 2.19t - 0.01\mathbb{1} \sin 3.62t + 1.79\sigma_x \cos 4.89t + 3.04\sigma_y \cos 2.69t$; for $n = 2$, $H = 1.01\sigma_z \mathbb{1} \cos 1.44t + 4.51\mathbb{1} \sin 4.55t - 2.7\sigma_y \sigma_z \sin 1.07t + 0.48\sigma_x \sigma_z \cos 2.26t$; for $n = 3$, $H = -1.281\sigma_x \mathbb{1} \cos 2.62t - 0.23\sigma_y \sigma_z \sin 3.75t - 1.341\sigma_x \sigma_x \sin 3.35t + 3.38\sigma_x \sigma_x \sigma_z \cos 2.34t$; for $n = 4$, $H = -0.41\mathbb{1} \sigma_z \sigma_x \sin 2.86t + 2.19\sigma_y \mathbb{1} \sigma_x \sigma_z \sin 1.38t - 0.87\sigma_y \sigma_x \sigma_x \sigma_z \sin 2.26t + 4.06\sigma_x \sigma_x \sigma_z \mathbb{1} \sin 1.76t$, where the shorthand used is $\mathbb{1} \sigma_x \mathbb{1} \equiv \mathbb{1} \otimes \sigma_x \otimes \mathbb{1}$. For example, trace fidelities with respect to the generalized CNOT (NOT or X-gate for $n = 1$, CNOT for $n = 2$, CCNOT for $n = 3$, and so on) are shown in the twin axis on the right. It can be seen that the step size of 10^{-1} leads to quick accumulation of error seen in the sharp peaks, but a step size of 10^{-2} is more stable with more than $O(10^3)$ times less prediction error.

model parameters $H_0(\zeta)^{(L)}$ with respect to the ground truth parameters H_0 . The prediction error $L_{\text{model}}(\mathcal{D}_{\text{val}})$ can be estimated using a validation data set \mathcal{D}_{val} and relates this observed validation loss to the Hamiltonian difference. Importantly, the inequality implies that the closeness in the propagator does not always translate to closeness in the Hamiltonian. Therefore, a model Hamiltonian can be locally a good fit for propagator predictions while still having a large Hamiltonian error $\|H_0^{(L)}(\zeta) - H_0\|$. So arbitrary closeness in terms of the Hamiltonian error need not be necessary for good unitary predictions. But conversely, if we can be certain that the model Hamiltonian is close to the system Hamiltonian, then the unitaries must be close. This suggests that a good guess (in the form of partial knowledge about the system) of the true Hamiltonian is useful in bounding the prediction errors.

We exploit this fact to learn the local Hamiltonian $H_0^{(L)}(\zeta)$ that approximates the dynamics of H_0 with respect to $U_{\mathcal{E}}$.

Qualitatively, we observe that Hamiltonian error, propagator validation, and training error are improved during training (i.e., the propagator loss on the validation set is predictive of Hamiltonian error). This can be seen in Fig. 8 for the noisy shot setting. But we also note in this example that the learned Hamiltonian $H_0^{(L)}(\zeta)$ is local, as seen from the Hamiltonian error plateauing at a nonzero value.

APPENDIX C: MONOTONIC IMPROVEMENT FOR MODEL RETURNS

We show that it is possible to improve the environment’s reward under an incorrect model ansatz in $\mathbf{M}_{\mathcal{E}}$. For that we need the following result from [27]:

Theorem 1 (Monotonic improvement for model-based returns [27]). Given k -branch rollout returns $\eta_{\text{branch}}(\pi)$ for a

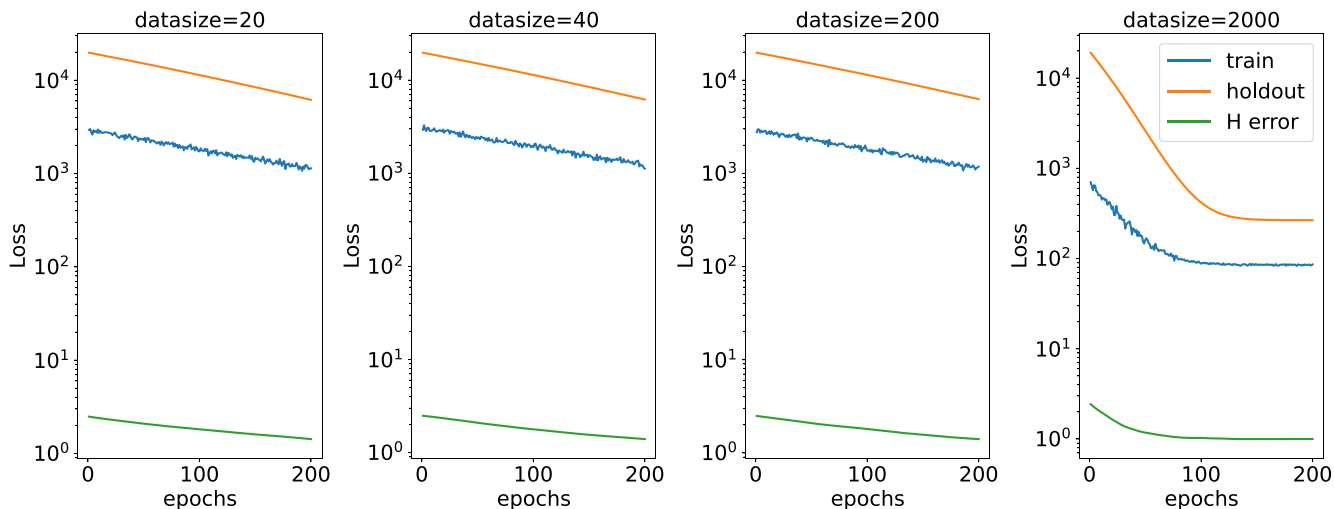


FIG. 8. The Hamiltonian error, unitary training $L_{\text{model}}(\mathcal{D}_{\text{train}})$, and validation (holdout) loss $L_{\text{model}}(\mathcal{D}_{\text{val}})$ as functions of training epochs for the two-qubit transmon unitary control problem with noisy measurements and $M = 10^5$. Data size denotes the number of single-step unitary transitions. The validation set is fixed to 5000 transitions under random policy actions \mathbf{a}_k . All three error measures improve as a function of training. Adding more training data appears to provide diminishing returns in predicting the local unitary dynamics.

policy π under the model, the true returns $\eta(\pi)$ are lower bounded,

$$\eta(\pi) \geq \eta_{\text{branch}}(\pi) - 2r_{\text{max}} \left(\frac{\gamma^{k+1} \epsilon_{\pi}}{(1-\gamma)^2} + \frac{\gamma^k + 2}{1-\gamma} \epsilon_{\pi} + \frac{k}{1-\gamma} (\epsilon_{\text{model}}) \right), \tag{C1}$$

where the returns η are defined as

$$\begin{aligned} \eta(\pi) &:= \mathbb{E}_{\pi} \left[\sum_{t=0}^{\infty} \gamma^t r_t(\mathbf{s}_t, \mathbf{a}_t) \right] \\ &= \mathbb{E}_{r_t \sim \mathcal{E}(\mathbf{s}_{t-1}, \mathbf{a}_t^{\pi})} \left[\sum_{t=0}^{\infty} \gamma^t r_t(\mathbf{s}_t, \mathbf{a}_t) \right]. \end{aligned} \tag{C2}$$

r_{max} is the maximum reward for an MDP transition; the policy error ϵ_{π} is the upper bound,

$$\epsilon_{\pi} \geq D_{\text{TV}}[\pi_D(\mathbf{s}, \mathbf{a}) \parallel \pi(\mathbf{s}, \mathbf{a})], \tag{C3}$$

where D_{TV} is the total variation distance and π_D is the data generating policy (i.e., the policy that generated the MDP data by interacting with the environment \mathcal{E}). The model error ϵ_{model} is the upper bound

$$\epsilon_{\text{model}} \geq \max_t \left(\mathbb{E}_{\mathbf{s} \sim \pi_D^{(t)}} \{ D_{\text{TV}} P_{\mathcal{E}}(\mathbf{s}'|\mathbf{s}, \mathbf{a}) \parallel P_M(\mathbf{s}'|\mathbf{s}, \mathbf{a}) \} \right), \tag{C4}$$

where $P_M(\mathbf{s}'|\mathbf{s}, \mathbf{a})$ is the MDP transition probability distribution under the model M that estimates the environment \mathcal{E} and likewise for $P_{\mathcal{E}}$. γ is the discount factor and k is the branch rollout length.

Proof. See the proof of Theorem 4.3 in [27]. ■

Informally, the theorem states that as long as the returns under the model η_{branch} are improved by at least the tolerance term $2r_{\text{max}}(\dots)$, then the returns under the environment η are guaranteed to improve. This also assumes that the policy π generating the model returns is reasonably close to the policy that interacts with the environment to generate the MDP data

that we use to compute the statistics including the returns. This policy error ϵ_{π} can be monitored online and controlled while running the algorithm by curtailing its training once it exceeds some tolerance threshold. Moreover, Ref. [27] shows that as long as the data-set size is large enough, the model error ϵ_m can be decoupled from the policy error ϵ_{π} . The optimal branch rollout length k^* is given by the minimizer of the tolerance. In practice, there are other considerations (e.g., the interplay between various hyperparameters) that need to be accounted for to determine k^* , so it is usually tuned numerically.

Using Theorem 1 for the ODE model, we can indirectly connect the Hamiltonian error using the validation loss $L_{\text{model}}(\mathcal{D}_{\text{val}})$ with ϵ_{model} . If the Hamiltonian error is small, then ϵ_{model} is small and the returns from the model and the environment are similar for any interacting policy π_{θ} . However, the returns need not be exactly the same and just need to be better than the tolerance provided by the term $-2r_{\text{max}}(\dots)$ in Eq. (C1) which is a function of ϵ_{model} . The tolerance is smaller for a more accurate model, and so less of an improvement of the model returns η_{branch} is necessary. The following lemma makes this idea concrete by applying Theorem 1 to our RL control problem setup.

Lemma 1 (Model error upper bound for the ODE model). If the model error ϵ_{model} upper bounds the risk,

$$\epsilon_{\text{model}} \geq \max_t \left(\mathbb{E}_{\mathbf{s} \sim \pi_D^{(t)}} \{ \mathbb{I}[\mathbf{M}_{\zeta}(\mathbf{s}, \mathbf{a}) \neq \mathcal{E}(\mathbf{s}, \mathbf{a})] \} \right), \tag{C5}$$

then it also upper bounds the unitary prediction error

$$\epsilon_{\text{model}} \geq \max_t \left(\mathbb{E}_{\mathbf{s} \sim \pi_D^{(t)}} \{ \|U_{\mathcal{E}}(\mathbf{s}, \mathbf{a}) - U_{\mathbf{M}_{\zeta}}(\mathbf{s}, \mathbf{a})\|_{\infty, t} \} \right), \tag{C6}$$

and the total variation distance between the model and environment probabilistic distributions,

$$\epsilon_{\text{model}} \geq \max_t \left(\mathbb{E}_{\mathbf{s} \sim \pi_D^{(t)}} \{ D_{\text{TV}}(P_{\mathcal{E}}(\mathbf{s}'|\mathbf{s}, \mathbf{a}) \parallel P_{\mathbf{M}_{\zeta}}(\mathbf{s}'|\mathbf{s}, \mathbf{a})) \} \right). \tag{C7}$$

Proof. Since the model M_ζ and the environment are both deterministic by assumption, we need to modify the lower bound on the model error ϵ_{model} in Theorem 1. We can replace the total variation distance between the two supposed distributions $P_\mathcal{E}, P_{M_\zeta}$ by an indicator variable $\mathbb{I}[M_\zeta(\mathbf{s}, \mathbf{a}) \neq \mathcal{E}(\mathbf{s}, \mathbf{a})]$ if $\mathbf{s}'_{M_\zeta} \neq \mathbf{s}'_\mathcal{E}$, which is 1 if the transitioned states do not match and 0 if they do. We can upper bound the total variation distance like this since $D_{\text{TV}}(P_\mathcal{E}, P_{M_\zeta}) = \sup_A |P_\mathcal{E}(A) - P_{M_\zeta}(A)| \leq 1$ in case the probabilities do not match and $D_{\text{TV}}(P_\mathcal{E}, P_{M_\zeta}) = 0$ when they match perfectly. Hence, there exists some ϵ_{model} such that

$$\begin{aligned} \epsilon_{\text{model}} &\geq \max_t (\mathbb{E}_{\mathbf{s} \sim \pi_D^{(t)}} \{\mathbb{I}[M_\zeta(\mathbf{s}, \mathbf{a}) \neq \mathcal{E}(\mathbf{s}, \mathbf{a})]\}) \\ &\geq \max_t (\mathbb{E}_{\mathbf{s} \sim \pi_D^{(t)}} \{D_{\text{TV}}[P_\mathcal{E}(\mathbf{s}'|\mathbf{s}, \mathbf{a}) \| P_{M_\zeta}(\mathbf{s}'|\mathbf{s}, \mathbf{a})]\}). \end{aligned}$$

The risk $\mathbb{E}_{\mathbf{s} \sim \pi_D^{(t)}} \{\mathbb{I}[M_\zeta(\mathbf{s}, \mathbf{a}) \neq \mathcal{E}(\mathbf{s}, \mathbf{a})]\}$ is essentially the fraction of unitaries that the model predicts incorrectly and is related to the unitary error in Proposition 2 by the fact that

$$\|U_\mathcal{E} - U_{M_\zeta}\|_{\infty, t} \leq \mathbb{I}[M_\zeta(\mathbf{s}, \mathbf{a}) \neq \mathcal{E}(\mathbf{s}, \mathbf{a})], \quad (C8)$$

provided that $\|U_\mathcal{E} - U_{M_\zeta}\|_{\infty, t}$ is normalized to be in $[0, 1]$. So we have

$$\begin{aligned} \mathbb{E}_{\mathbf{s} \sim \pi_D^{(t)}} \{\|U_{\mathcal{E}(\mathbf{s}, \mathbf{a})} - U_{M_\zeta(\mathbf{s}, \mathbf{a})}\|_{\infty, t}\} \\ \leq \mathbb{E}_{\mathbf{s} \sim \pi_D^{(t)}} \{\mathbb{I}[M_\zeta(\mathbf{s}, \mathbf{a}) \neq \mathcal{E}(\mathbf{s}, \mathbf{a})]\}. \end{aligned} \quad (C9)$$

So ϵ_{model} upper bounds the expected unitary error if and only if ϵ_{model} upper bounds the expected risk in the unitary prediction error. ■

APPENDIX D: HOW MUCH DATA ARE NEEDED FOR MODEL TRAINING?

A hallmark for a good ansatz for the model M_ζ estimating the dynamics of the controllable system would be less demand of supervised learning MDP data needed for low prediction error.

We consider the Hamiltonian error, unitary train, and holdout error. Hamiltonian error δ is the spectral norm error between the learned and true system Hamiltonian. The others are mean-squared errors. Cross-validation is used to estimate the model’s generalization ability on a holdout data set of unseen random unitary data, also sampled from the MDP transitions and collected by the policy π during training.

As seen from Fig. 8, for the two-qubit transmon control problem, for very small data-set sizes comprising 20–200

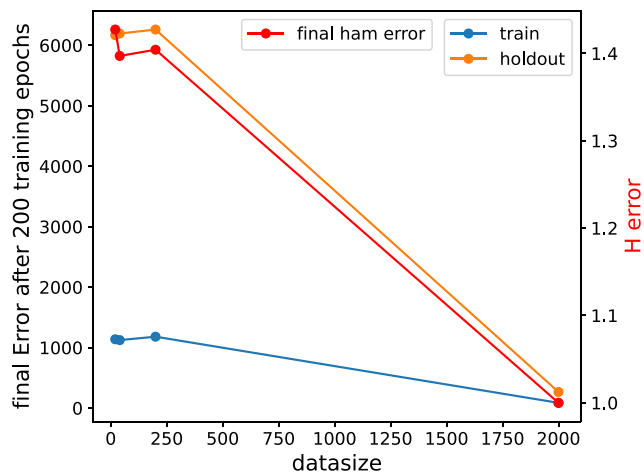


FIG. 9. Effect of training data size on model generalization metrics: Hamiltonian error, unitary training $L_{\text{model}}(\mathcal{D}_{\text{train}})$, and validation (holdout) loss $L_{\text{model}}(\mathcal{D}_{\text{val}})$ for noisy single-shot measurement-based unitary control of the transmon.

unitary transitions, the single step unitary prediction error is large compared to training with about 2000 unitaries or about 100 full length pulses with 20 time steps, though the decrease in error is diminishing with data-set size. All errors are in agreement across the data sets over 200 training epochs. This is further corroborated by Fig. 9 where the final errors after 200 epochs are plotted. There is a reduction in the final errors for the 2000 data-set size, but the improvement is diminishing in magnitude and plateaus at this loss for larger data-set sizes. This is still much less than what was required to train a neural network model for M_ζ during the initial stages of our research where the training data-set size needed to be of the order of 10^6 . Moreover, these experiments provide us with an idea of what data-set size to use to train the model M_ζ by setting the number of initial exploration MDP transitions to add to the policy’s buffer for the transmon control problem. We also adopted multiple training phases to continuously train M_ζ using fresh batches of training data collected by the policy.

APPENDIX E: LEVERAGING THE LEARNED HAMILTONIAN FOR THE TWO-QUBIT NV CENTER

Similar to the results found in Sec. IV C, here we report the structural differences between the learned and target Hamiltonians for the two-qubit NV center.

The matrix difference between the true H_0 and learned Hamiltonian $H_0(\zeta)$ is

$$H - H_0(\zeta) = \begin{bmatrix} 0.0116 & 0.0013i & -0.0001 - 0.0002i & -0.0007 \\ -0.0013i & -0.0111 & -0.0001 + 0.0002i & 0.0003 + 0.0003i \\ -0.0001 + 0.0002i & 0.0001 + 0.0002i & -0.0108 & -0.0005 - 0.0002i \\ -0.0007 & 0.0003 - 0.0003i & -0.0005 + 0.0002i & -0.013 \end{bmatrix}.$$

Moreover, the nonlinear relationship between the model prediction errors and the spectral norm error δ or the mean-squared Pauli expectation value error is confirmed as before in Fig. 10(a). Local and global trajectory differences under a

random control pulse and the results of using GRAPE on RL controllers are shown in Figs. 10(b) and 10(c), respectively. The learned Hamiltonian is able to improve the controller fidelities to greater than 0.999.

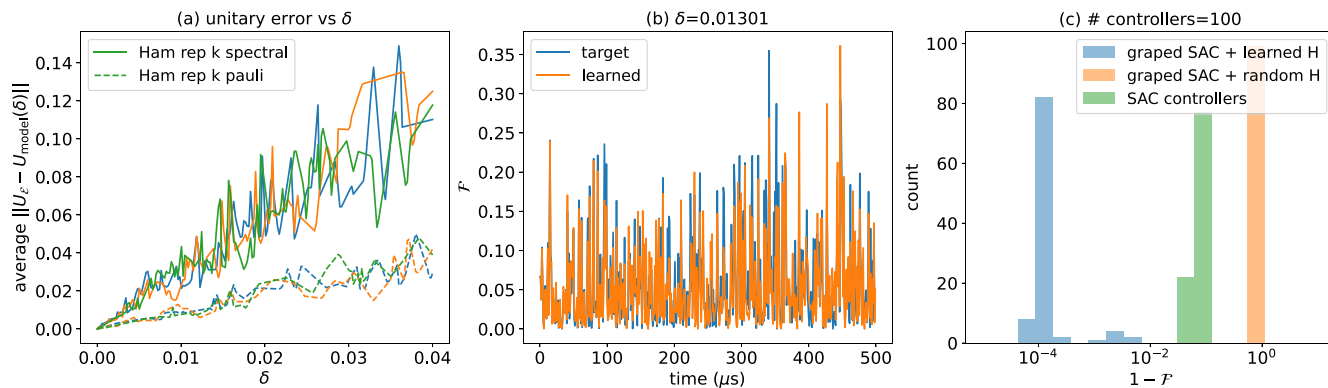


FIG. 10. (a) The nonlinear relationship between the prediction error $\|U_\xi - U_{\text{model}}\|$ and Hamiltonian spectral norm error or mean-squared Pauli expectation value error δ for the two-qubit NV center Hamiltonian. For the same 1000 random control pulses, we evaluate the average unitary prediction error of \mathbf{M}_ξ with increasing δ for three different uniform randomly sampled two-qubit Hamiltonians $H_0(\xi)$. (b) Local and global unitary trajectories: \mathcal{F} as a function of a random control pulse with either the learned $H_0(\xi)$ or true H_0 . The learned trajectories and global trajectory overlap less with increasing time with the spectral norm error of $\delta = 0.01301$ and a global phase factor $\text{Tr}[H - H_0(\xi)]$ of ~ 0.01 . (c) The learned $H_0(\xi)$ can be leveraged using GRAPE to further optimize the fidelities of LH-MBSAC’s controllers. Repeating the procedure in Sec. IV C yields fidelities of greater than 0.999.

APPENDIX F: THREE-QUBIT TRANSMON CONTROL PROBLEM

In this Appendix, we discuss the issue of scalability of LH-MBSAC’s performance related to the three-qubit transmon control problem in Sec. IV E in detail.

Working with two level systems, we extend the two-qubit transmon Hamiltonian to its three-qubit version $H_{\text{tra}}^{(3)}$. The system part generalizes trivially. For the control part $H_{\text{tra}_c}^{(3)}$, we generalize the cross-resonance interaction presented in Ref. [72] to construct the following time-dependent part of the three-qubit transmon Hamiltonian:

$$\frac{H_{\text{tra}_c}^{(3)}(t)}{\hbar} = \sum_{l=1}^3 (a_l(t)(Z_l X_{l+1} + X_{l+1} + Y_{l+1} + Z_l) + b_l(t)(X_l Z_{l+1} + X_l + Y_l + Z_{l+1})), \quad (\text{F1})$$

where $a_l(t)$, $b_l(t)$ are the real drive amplitudes and X_l , Y_l , Z_l are the corresponding Pauli operators on the l th qubit.

To start, we mention our hyperparameter strategy. Only an initial hyperparameter search is performed for the two-qubit transmon control problem, and we were successfully able to transfer the same hyperparameters to all problems in the paper that were studied, including the ones presented in Fig. 2.

It is a desirable property for the stability of RL algorithms to be robust to hyperparameter changes for different target problems, which we found to be the case. The search was only conducted for the model-free SAC since LH-MBSAC is just a model-based augmentation of the underlying SAC algorithm so there is no strong reason for the hyperparameters to fail to transfer.

However, for the three-qubit transmon control problem, we encountered issues and had to repeat the search. This was extensive, and we focused on the following: more initial exploration data, using bigger layer sizes for the policy and value function neural networks, changing the learning and update rates for the policy and value functions, among other things. An extremely thorough search is difficult since

the problem is more computationally challenging, and it is hard to determine when to terminate the training during a trial run that necessarily needs to be premature during the hyperparameter search. Please see the accompanying code for the list of hyperparameters we searched over using Bayesian optimization in `tune_hypers.py` along with some results in the `hyper_tests` folder.

Furthermore, we make observations that make this issue seem less like a hyperparameter issue and more like an optimization landscape problem:

(i) The values and the gradients for policy and value functions that saturate are both stuck in suboptimal extrema and ultimately we get stuck at a prematurely optimized reward function. This is illustrated in Fig. 11. Essentially, SAC gets

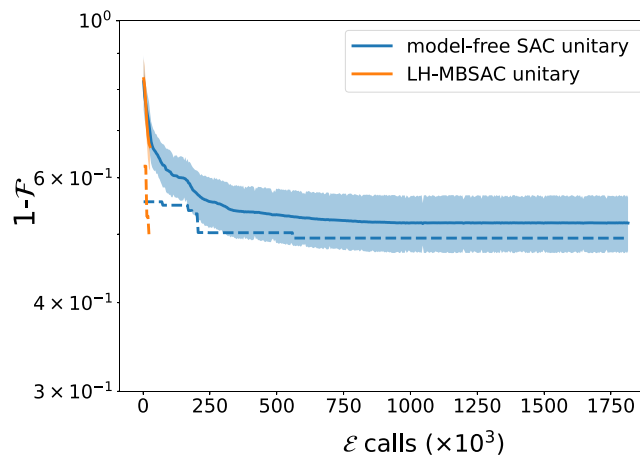


FIG. 11. Noiseless unitary sample complexity for the three-qubit transmon where the target gate is the Toffoli gate. Since LH-MBSAC is based on SAC, the latter’s training curves are obtained first to see if it viably solves the problem, and it was trained for much longer, i.e., in the order of millions of samples as seen in Fig. 11. Mean (solid) and maximum fidelities (dashed) saturate as the policy and value function gradients and outputs saturate due to the agent getting stuck in a suboptimal extremum of the optimization landscape.

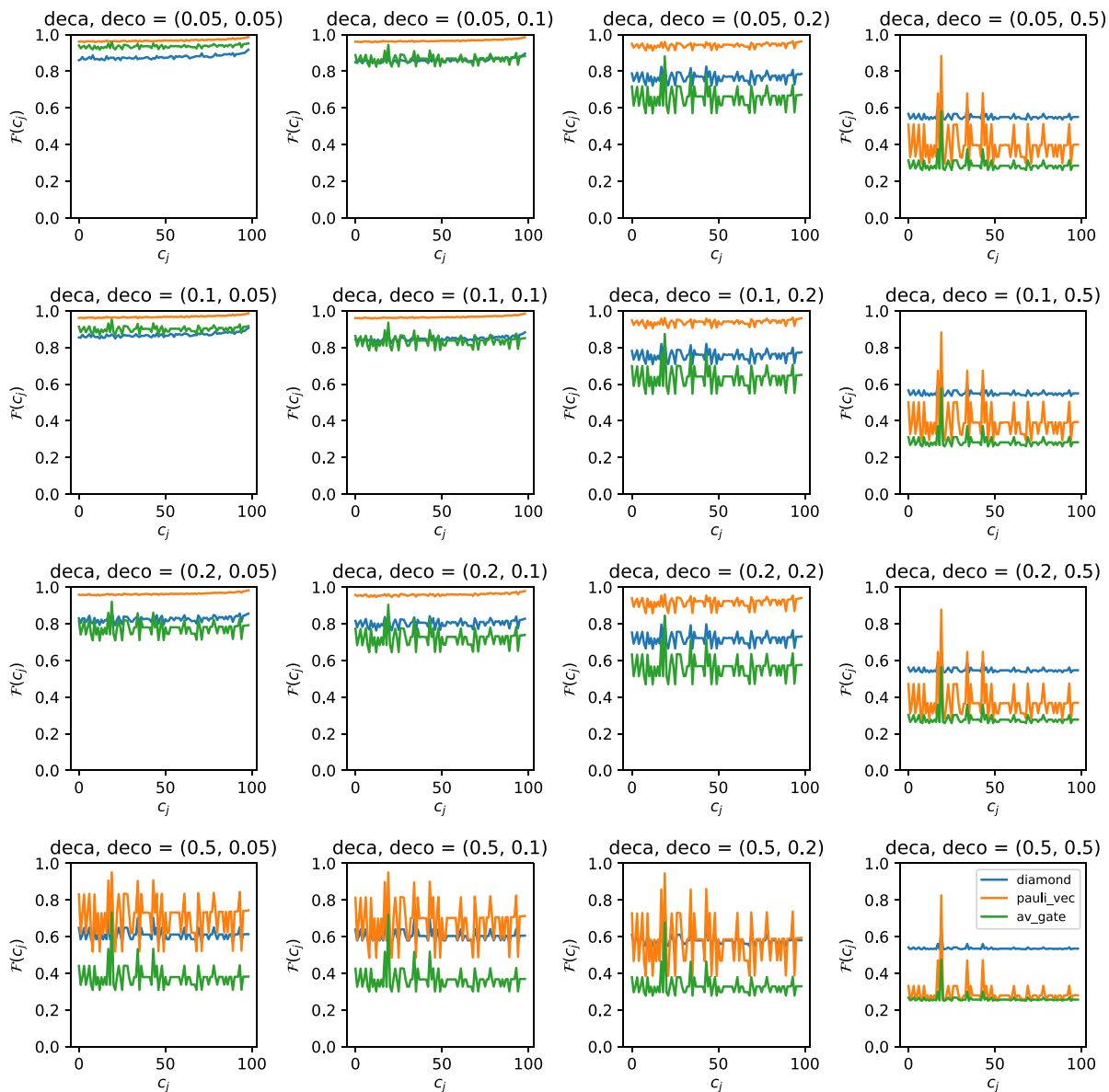


FIG. 12. This figure shows how much the fidelity measures relate to one another as the dissipation strength varies in terms of the decoherence and the decay coefficients in Eq. (6) for the Lindbladian l_d operators. Here, deca, deco refer to inverse decay and decoherence rates $2/T_1^*$, $2/T_1$, respectively, for the l th qubit measured in MHz. The x -axis refers to a controller c_j obtained for the two-qubit transmon gate control problem with single-shot measurement noise where the target is the CNOT gate. The controllers are in random order with respect to the fidelity, but the ordering is preserved across each subfigure. The number of single-shot measurements is 10^6 , and diamond, pauli_vec, av_gate refer to the diamond norm fidelity [64], the generalized state fidelity [48], and the average gate fidelity [73], respectively.

stuck in a loop mining medium level fidelities and its policy outputs saturate on the extremes of the control amplitudes. It was already detailed in Sec. IV E that RL pulses are biased towards maintaining high intermediate fidelities due to the nature of the MDP used in the paper. Figure 6 shows example pulses found by RL versus GRAPE for the two-qubit transmon, confirming this.

(ii) Since we have the model Hamiltonian, we insert it into GRAPE initialized with the highest fidelity SAC controller values, and it also gets stuck (at slightly better fidelities).

Despite these issues, the system Hamiltonian is still learned. It can be inserted into GRAPE with uniform random initialization of control pulse parameters to achieve fidelities of over 0.999.

APPENDIX G: COMPARISON OF FIDELITIES FOR LINDBLADIAN DYNAMICS

We study the agreement between three different fidelity measures of realized noisy gates on open systems with Lindblad decay and decoherence for the two-qubit transmon gate

control problem. The fidelity measures are the diamond norm fidelity [64], the generalized state fidelity [48], and the average gate fidelity [73]. The diamond norm fidelity, derived from the diamond norm or the completely bounded trace norm, is the most expensive to compute as it involves solving a convex optimization problem:

$$\begin{aligned} \mathcal{F}_\diamond(\Phi(\mathbf{u}(t), t), \Phi_{\text{target}}) &= 1 - \|\Phi(\mathbf{u}(t), t) - \Phi_{\text{target}}\|_\diamond \\ &= 1 - \max_\rho \|\Phi(\mathbf{u}(t), t) \circ \rho - \Phi_{\text{target}} \circ \rho\|_1, \end{aligned} \quad (\text{G1})$$

where the maximization is over the space of all density matrices ρ . This can be done by solving an equivalent semidefinite program [74], $0.5 \leq \mathcal{F}_\diamond(\Phi(\mathbf{u}(t), t)) \leq 1$.

To study the sensitivities of the measures to dissipation and their agreement with respect to each other, we consider low, medium, and high dissipation regimes. We evaluate 100 of our controllers found for the noisy single-shot measurements setting of the two-qubit transmon in these regimes. The results are plotted in Fig. 12. Here, deca and deco refer to inverse decoherence and decay rates $2/T_1^*$, $2/T_1$, respectively, for the l th

qubit, measured in MHz. We renormalize the trace of the realized operator $\Phi(\mathbf{u}(t), t)$ during our experiments, as is standard practice. Due to the exhaustive nature of its computation, \mathcal{F}_\diamond is the most sensitive to noise and loss of coherence out of all the measures. The generalized state fidelity is the least sensitive, and the average gate fidelity falls in the middle. For very low to medium dissipation levels, e.g., (0.05, 0.05), (0.05, 0.1), or (0.05, 0.2) for the pair (deca, deco), the generalized state fidelity is near perfect while the gate and diamond norm fidelities are more sensitive and closer to 0.9. For this reason, in Sec. IV D, we chose to use the diamond norm fidelity to more accurately gauge controller performance—this was especially true for the low dissipation regime results.

As a side note, some controllers shown in Fig. 12 are more robust to dissipation than others, as revealed by the noisy variation across the controller index versus fidelity plot. The controllers are not ordered, so the fidelity in the zero dissipation regime has some noise/variation as seen for deca, deco = (0.05, 0.05). Across all the subfigures, the robustness is captured by all the fidelity measures where the variation magnitudes and positions are more or less aligned.

-
- [1] C. P. Koch, U. Boscain, T. Calarco, G. Dirr, S. Filipp, S. J. Glaser, R. Kosloff, S. Montangero, T. Schulte-Herbrüggen, D. Sugny, and F. K. Wilhelm, Quantum optimal control in quantum technologies. Strategic report on current status, visions and goals for research in europe, *EPJ Quantum Technol.* **9**, 19 (2022).
- [2] P. Krantz, M. Kjaergaard, F. Yan, T. P. Orlando, S. Gustavsson, and W. D. Oliver, A quantum engineer’s guide to superconducting qubits, *Appl. Phys. Rev.* **6**, 021318 (2019).
- [3] D. Gottesman, Quantum fault tolerance in small experiments, [arXiv:1610.03507](https://arxiv.org/abs/1610.03507).
- [4] R. Harper and S. T. Flammia, Fault-tolerant logical gates in the IBM quantum experience, *Phys. Rev. Lett.* **122**, 080504 (2019).
- [5] J. M. Chow, J. M. Gambetta, E. Magesan, D. W. Abraham, A. W. Cross, B. R. Johnson, N. A. Masluk, C. A. Ryan, J. A. Smolin, S. J. Srinivasan *et al.*, Implementing a strand of a scalable fault-tolerant quantum computing fabric, *Nat. Commun.* **5**, 4015 (2014).
- [6] I. Khalid, C. Weidner, E. A. Jonckheere, S. G. Schirmer, and F. C. Langbein, Reinforcement learning vs. gradient-based optimisation for robust energy landscape control of spin-1/2 quantum networks, in *60th IEEE Conference on Decision and Control (CDC)* (IEEE, Piscataway, NJ, 2021), pp. 4133–4139.
- [7] N. Khaneja, T. Reiss, C. Kehlet, T. Schulte-Herbrüggen, and S. J. Glaser, Optimal control of coupled spin dynamics: Design of nmr pulse sequences by gradient ascent algorithms, *J. Magn. Reson.* **172**, 296 (2005).
- [8] D. M. Reich, M. Ndong, and C. P. Koch, Monotonically convergent optimization in quantum control using krotov’s method, *J. Chem. Phys.* **136**, 104103 (2012).
- [9] S. Machnes, U. Sander, S. J. Glaser, P. de Fouquières, A. Grusly, S. Schirmer, and T. Schulte-Herbrüggen, Comparing, optimizing, and benchmarking quantum-control algorithms in a unifying programming framework, *Phys. Rev. A* **84**, 022305 (2011).
- [10] N. Wittler, F. Roy, K. Pack, M. Werninghaus, A. S. Roy, D. J. Egger, S. Filipp, F. K. Wilhelm, and S. Machnes, Integrated tool set for control, calibration, and characterization of quantum devices applied to superconducting qubits, *Phys. Rev. Appl.* **15**, 034080 (2021).
- [11] M. Y. Niu, S. Boixo, V. N. Smelyanskiy, and H. Neven, Universal quantum control through deep reinforcement learning, *npj Quantum Inf.* **5**, 33 (2019).
- [12] I. Khalid, C. A. Weidner, E. A. Jonckheere, S. G. Schirmer, and F. C. Langbein, Statistically characterizing robustness and fidelity of quantum controls and quantum control algorithms, *Phys. Rev. A* **107**, 032606 (2023).
- [13] M. Dalggaard, F. Motzoi, J. J. Sørensen, and J. Sherson, Global optimization of quantum dynamics with alphazero deep exploration, *npj Quantum Inf.* **6**, 6 (2020).
- [14] V. V. Sivak, A. Eickbusch, H. Liu, B. Royer, I. Tsioutsios, and M. H. Devoret, Model-free quantum control with reinforcement learning, *Phys. Rev. X* **12**, 011059 (2022).
- [15] M. Bukov, A. G. R. Day, D. Sels, P. Weinberg, A. Polkovnikov, and P. Mehta, Reinforcement learning in different phases of quantum control, *Phys. Rev. X* **8**, 031086 (2018).
- [16] X.-D. Yang, C. Arenz, I. Pelczar, Q.-M. Chen, R.-B. Wu, X. Peng, and H. Rabitz, Assessing three closed-loop learning algorithms by searching for high-quality quantum control pulses, *Phys. Rev. A* **102**, 062605 (2020).
- [17] F. Schäfer, M. Kloc, C. Bruder, and N. Lörch, A differentiable programming method for quantum control, *Mach. Learn.: Sci. Technol.* **1**, 035009 (2020).
- [18] F. Schäfer, P. Sekatski, M. Koppenhöfer, C. Bruder, and M. Kloc, Control of stochastic quantum dynamics by differentiable programming, *Mach. Learn.: Sci. Technol.* **2**, 035004 (2021).
- [19] M. H. Goerz, S. C. Carrasco, and V. S. Malinovsky, Quantum optimal control via semi-automatic differentiation, *Quantum* **6**, 871 (2022).
- [20] N. Leung, M. Abdelhafez, J. Koch, and D. Schuster, Speedup for quantum optimal control from automatic differentiation

- based on graphics processing units, *Phys. Rev. A* **95**, 042318 (2017).
- [21] R. S. Sutton and A. G. Barto, *Reinforcement Learning: An Introduction* (MIT press, Cambridge, MA, 2018).
- [22] Y. Baum, M. Amico, S. Howell, M. Hush, M. Liuzzi, P. Mundada, T. Merkh, A. R. R. Carvalho, and M. J. Biercuk, Experimental deep reinforcement learning for error-robust gate-set design on a superconducting quantum computer, *PRX Quantum* **2**, 040324 (2021).
- [23] V. Sivak, A. Eickbusch, B. Royer, S. Singh, I. Tsioutsios, S. Ganjam, A. Miano, B. Brock, A. Ding, L. Frunzio *et al.*, Real-time quantum error correction beyond break-even, *Nature (London)* **616**, 50 (2023).
- [24] L. Ding, M. Hays, Y. Sung, B. Kannan, J. An, A. D. Paolo, A. H. Karamlou, T. M. Hazard, K. Azar, D. K. Kim, B. M. Niedzielski, A. Melville, M. E. Schwartz, J. L. Yoder, T. P. Orlando, S. Gustavsson, J. A. Grover, K. Serniak, and W. D. Oliver, High-fidelity, frequency-flexible two-qubit fluxonium gates with a transmon coupler, [arXiv:2304.06087](https://arxiv.org/abs/2304.06087).
- [25] R. S. Sutton, Dyna, an integrated architecture for learning, planning, and reacting, *ACM SIGART Bull.* **2**, 160 (1991).
- [26] K. Chua, R. Calandra, R. McAllister, and S. Levine, Deep reinforcement learning in a handful of trials using probabilistic dynamics models, in *Advances in Neural Information Processing Systems*, edited by S. Bengio, H. Wallach, H. Larochelle, K. Grauman, N. Cesa-Bianchi, and R. Garnett (Curran Associates, Montreal, Canada, 2018), Vol. 31.
- [27] M. Janner, J. Fu, M. Zhang, and S. Levine, When to trust your model: Model-based policy optimization, in *Advances in Neural Information Processing Systems* (Curran Associates, Vancouver, Canada, 2019), Vol. 32.
- [28] H. P. Van Hasselt, M. Hessel, and J. Aslanides, When to use parametric models in reinforcement learning? in *Advances in Neural Information Processing Systems* (Curran Associates, Vancouver, Canada, 2019), Vol. 32.
- [29] R. T. Q. Chen, Y. Rubanova, J. Bettencourt, and D. K. Duvenaud, Neural ordinary differential equations, in *Advances in Neural Information Processing Systems*, edited by S. Bengio, H. Wallach, H. Larochelle, K. Grauman, N. Cesa-Bianchi, and R. Garnett (Curran Associates, Montreal, Canada, 2018), Vol. 31.
- [30] E. A. Coddington and N. Levinson, *Theory of Ordinary Differential Equations* (Tata McGraw-Hill Education, New York, USA, 1955).
- [31] E. Dupont, A. Doucet, and Y. W. Teh, Augmented neural ODEs, in *Advances in Neural Information Processing Systems*, edited by H. Wallach, H. Larochelle, A. Beygelzimer, F. d'Alché-Buc, E. Fox, and R. Garnett (Curran Associates, Vancouver, Canada, 2019), Vol. 32.
- [32] H. Yan, J. Du, V. Y. F. Tan, and J. Feng, On robustness of neural ordinary differential equations, [arXiv:1910.05513](https://arxiv.org/abs/1910.05513).
- [33] M. M. Bronstein, J. Bruna, T. Cohen, and P. Veličković, Geometric deep learning: Grids, groups, graphs, geodesics, and gauges, [arXiv:2104.13478](https://arxiv.org/abs/2104.13478).
- [34] T. Haarnoja, A. Zhou, P. Abbeel, and S. Levine, Soft actor-critic: Off-policy maximum entropy deep reinforcement learning with a stochastic actor, in *International Conference on Machine Learning* (PMLR, Stockholm, Sweden, 2018), pp. 1861–1870.
- [35] S. S. Hegde, J. Zhang, and D. Suter, Efficient quantum gates for individual nuclear spin qubits by indirect control, *Phys. Rev. Lett.* **124**, 220501 (2020).
- [36] E. Magesan and J. M. Gambetta, Effective Hamiltonian models of the cross-resonance gate, *Phys. Rev. A* **101**, 052308 (2020).
- [37] M. Clouâtre, M. J. Khojasteh, and M. Z. Win, Model-predictive quantum control via Hamiltonian learning, *Trans. Quantum Eng.* **3**, 1 (2022).
- [38] A. Dutkiewicz, T. E. O'Brien, and T. Schuster, The advantage of quantum control in many-body Hamiltonian learning, [arXiv:2304.07172](https://arxiv.org/abs/2304.07172).
- [39] H.-P. Breuer, F. Petruccione *et al.*, *The Theory of Open Quantum Systems* (Oxford University Press on Demand, 2002).
- [40] F. F. Floether, P. De Fouquieres, and S. G. Schirmer, Robust quantum gates for open systems via optimal control: Markovian versus non-Markovian dynamics, *New J. Phys.* **14**, 073023 (2012).
- [41] C. J. Wood, J. D. Biamonte, and D. G. Cory, Tensor networks and graphical calculus for open quantum systems, *Quant. Inf. Comput.* **15**, 0579 (2015).
- [42] A. Lichnerowicz, *Elements of Tensor Calculus* (Courier Dover, Mineola, New York, USA, 2016).
- [43] M.-D. Choi, Completely positive linear maps on complex matrices, *Lin. Alg. Appl.* **10**, 285 (1975).
- [44] A. Jamiolkowski, Linear transformations which preserve trace and positive semidefiniteness of operators, *Rep. Math. Phys.* **3**, 275 (1972).
- [45] J. B. Altepeter, D. Branning, E. Jeffrey, T. C. Wei, P. G. Kwiat, R. T. Thew, J. L. O'Brien, M. A. Nielsen, and A. G. White, Ancilla-assisted quantum process tomography, *Phys. Rev. Lett.* **90**, 193601 (2003).
- [46] R. A. Bertlmann and P. Krammer, Bloch vectors for qudits, *J. Phys. A* **41**, 235303 (2008).
- [47] F. Sauvage and F. Mintert, Optimal quantum control with poor statistics, *PRX Quantum* **1**, 020322 (2020).
- [48] S. T. Flammia and Y.-K. Liu, direct fidelity estimation from few Pauli measurements, *Phys. Rev. Lett.* **106**, 230501 (2011).
- [49] B. D. Ziebart, A. L. Maas, J. A. Bagnell, A. K. Dey *et al.*, Maximum entropy inverse reinforcement learning, in *Aaai* (Association for the Advancement of Artificial Intelligence, Chicago, 2008), Vol. 3, pp. 1433–1438.
- [50] L. Younes, *Shapes and Diffeomorphisms*, Applied Mathematical Sciences Vol. 171 (Springer, New York, USA, 2010).
- [51] R. Howard, The Gronwall inequality, Lecture notes in Physics (1998).
- [52] F. Frank, T. Unden, J. Zoller, R. S. Said, T. Calarco, S. Montangero, B. Naydenov, and F. Jelezko, Autonomous calibration of single spin qubit operations, *npj Quantum Inf.* **3**, 48 (2017).
- [53] A. Cross, The IBM Q experience and QISKit open-source quantum computing software, in *APS March Meeting Abstracts* (APS, 2018), Vol. 2018, pp. L58–003.
- [54] T. D. Kühner, S. R. White, and H. Monien, One-dimensional Bose-Hubbard model with nearest-neighbor interaction, *Phys. Rev. B* **61**, 12474 (2000).
- [55] A. Paszke, S. Gross, F. Massa, A. Lerer, J. Bradbury, G. Chanan, T. Killeen, Z. Lin, N. Gimelshein, L. Antiga *et al.*, Pytorch: An imperative style, high-performance deep learning library, in *Advances in Neural Information Processing Systems* (Curran Associates, Vancouver, Canada, 2019), Vol. 32.

- [56] M. Mohri, A. Rostamizadeh, and A. Talwalkar, *Foundations of Machine Learning* (MIT press, Cambridge, MA, 2018).
- [57] H.-Y. Huang, R. Kueng, and J. Preskill, Predicting many properties of a quantum system from very few measurements, *Nat. Phys.* **16**, 1050 (2020).
- [58] M. A. Nielsen and I. L. Chuang, *Quantum Computation and Quantum Information* (Cambridge University Press, 2010).
- [59] D. Burgarth, P. Facchi, G. Gramegna, and K. Yuasa, One bound to rule them all: From adiabatic to zeno, *Quantum* **6**, 737 (2022).
- [60] A. Anshu, S. Arunachalam, T. Kuwahara, and M. Soleimanifar, Sample-efficient learning of interacting quantum systems, *Nat. Phys.* **17**, 931 (2021).
- [61] J. Haah, R. Kothari, and E. Tang, Optimal learning of quantum Hamiltonians from high-temperature Gibbs states, in *IEEE 63rd Annual Symposium on Foundations of Computer Science (FOCS)* (IEEE, Piscataway, NJ, 2022), pp. 135–146.
- [62] T. J. Evans, R. Harper, and S. T. Flammia, Scalable Bayesian Hamiltonian learning, [arXiv:1912.07636](https://arxiv.org/abs/1912.07636).
- [63] A. Izmalkov, S. H. W. van der Ploeg, S. N. Shevchenko, M. Grajcar, E. Il'ichev, U. Hübner, A. N. Omelyanchouk, and H.-G. Meyer, Consistency of ground state and spectroscopic measurements on flux qubits, *Phys. Rev. Lett.* **101**, 017003 (2008).
- [64] G. Benenti and G. Strini, Computing the distance between quantum channels: Usefulness of the fano representation, *J. Phys. B* **43**, 215508 (2010).
- [65] A. Valenti, E. van Nieuwenburg, S. Huber, and E. Greplova, Hamiltonian learning for quantum error correction, *Phys. Rev. Res.* **1**, 033092 (2019).
- [66] H.-Y. Huang, Y. Tong, D. Fang, and Y. Su, Learning many-body Hamiltonians with Heisenberg-limited scaling, *Phys. Rev. Lett.* **130**, 200403 (2023).
- [67] M. Hausknecht and P. Stone, Deep recurrent Q-learning for partially observable MDPs, in *AAAI Fall Symposium Series*, [arXiv:1507.06527](https://arxiv.org/abs/1507.06527).
- [68] H.-Y. Huang, S. Chen, and J. Preskill, Learning to predict arbitrary quantum processes, [arXiv:2210.14894](https://arxiv.org/abs/2210.14894).
- [69] https://github.com/ergodic/transmon_public.
- [70] E. Süli and D. F. Mayers, *An Introduction to Numerical Analysis* (Cambridge University Press, 2003).
- [71] P. Virtanen, R. Gommers, T. E. Oliphant, M. Haberland, T. Reddy, D. Cournapeau, E. Burovski, P. Peterson, W. Weckesser, J. Bright *et al.*, SciPy 1.0: Fundamental algorithms for scientific computing in python, *Nat. Methods* **17**, 261 (2020).
- [72] S. Sheldon, E. Magesan, J. M. Chow, and J. M. Gambetta, Procedure for systematically tuning up cross-talk in the cross-resonance gate, *Phys. Rev. A* **93**, 060302(R) (2016).
- [73] A. Uhlmann, Fidelity and concurrence of conjugated states, *Phys. Rev. A* **62**, 032307 (2000).
- [74] J. Watrous, Semidefinite programs for completely bounded norms, [arXiv:0901.4709](https://arxiv.org/abs/0901.4709).